Progress in Oceanography 219 (2023) 103162

Contents lists available at ScienceDirect

Progress in Oceanography

journal homepage: www.elsevier.com/locate/pocean

Hydrography, inorganic nutrients and chlorophyll *a* linked to sea ice cover in the Atlantic Water inflow region north of Svalbard

Angelika H.H. Renner [a,*], Allison Bailey [b], Marit Reigstad [c], Arild Sundfjord [b], Melissa Chierici [a], Elizabeth M. Jones [a]

[a] Institute of Marine Research, Tromsø, Norway
[b] Norwegian Polar Institute, Tromsø, Norway
[c] UiT The Arctic University of Norway, Tromsø, Norway

ARTICLE INFO

Keywords:
Atlantic Water Boundary Current
Stratification
Nutrient re-supply
Phytoplankton
Primary production
Sea ice
Arctic Ocean
Barents Sea
Svalbard

ABSTRACT

Changes in the inflow of Atlantic Water (AW) and its properties to the Arctic Ocean bring more warm water, contribute to sea ice decline, promote borealisation of marine ecosystems, and affect biological and particularly primary productivity in the Eurasian Arctic Ocean. One of the two branches of AW inflow follows the shelf break north of Svalbard, where it dominates oceanographic conditions, bringing in heat, salt, nutrients and organisms. However, the interplay with sea ice and Polar Surface Water (PSW) determines the supply of nutrients to the euphotic layer especially northeast of Svalbard where AW subducts below PSW. In an effort to build up a time series monitoring the key characteristics of the AW inflow, repeat sampling of hydrography, macronutrients (nitrate, phosphate and silicate), and chlorophyll *a* (chl *a*) was undertaken along a transect across the AW inflow at 31°E, 81.5°N since 2012 — first during late summer and in later years during early winter. Such time series are scarce but invaluable for investigating the range of variability in hydrography and nutrient concentrations. We investigate linkages between late summer hydrographic conditions and nutrient concentrations along the transect and the preceding seasonal dynamics of surface chl *a* and sea ice cover in the region north of Svalbard. We find large interannual variability in hydrography, nutrients and chl *a*, indicating varying levels of nutrient drawdown by primary producers over summer. Sea ice conditions varied considerably between the years, impacting upper ocean stratification, light availability and potential wind-driven mixing, with a strong potential for steering chl *a* concentration over the productive season. Early winter measurements show variable efficiency of nutrient re-supply through vertical mixing when stratification was low, related to autumn wind forcing and sea ice conditions. While this re-supply elevates nutrient levels sufficiently for primary production, it likely happens too late in the season when light levels are already low, limiting the potential for autumn blooms. Such multidisciplinary observations provide insight into the interplay between physical, chemical and biological drivers in the marine environment and are key to understanding ongoing and future changes, especially at this entrance to the central Arctic Ocean.

1. Introduction

The physical environment of the Arctic Ocean is changing rapidly with ongoing climate change; air temperatures are rising faster than the global average (Previdi et al., 2021; Rantanen et al., 2022), sea ice cover is declining and thinning (Stroeve and Notz, 2018), freshwater content in the ocean surface layer has been increasing in the central Arctic and decreasing on the shelves (Timmermans and Marshall, 2020; Solomon et al., 2021), heat content and salinity are increasing due to enhanced inflow from lower latitudes and increased solar warming (Polyakov et al., 2020; Timmermans and Marshall, 2020), and circulation patterns are changing, especially connected to altered wind and sea ice drift patterns (Wang and Danilov, 2022). These changes have large impacts on the marine ecosystem (Pörtner et al., 2019; Ingvaldsen et al., 2021).

Sea ice cover immediately affects the light regime in the upper ocean: thinner ice with less snow on top, smaller ice floes and larger open water areas allow for more light to reach the marine environment, where it can be used by phytoplankton for primary production (e.g., Nicolaus et al., 2012; Assmy et al., 2017; Castellani et al., 2022). The recent decrease in Arctic sea ice concentration, extent and thickness leading to a lengthening of the open-water season and a greater open-water pelagic phytoplankton habitat, has positively impacted primary productivity in the Arctic Ocean (Arrigo and van Dijken, 2015; Ardyna and Arrigo, 2020). Satellite-based studies estimate

* Corresponding author.
E-mail address: angelika.renner@hi.no (A.H.H. Renner).

https://doi.org/10.1016/j.pocean.2023.103162

Available online 4 November 2023

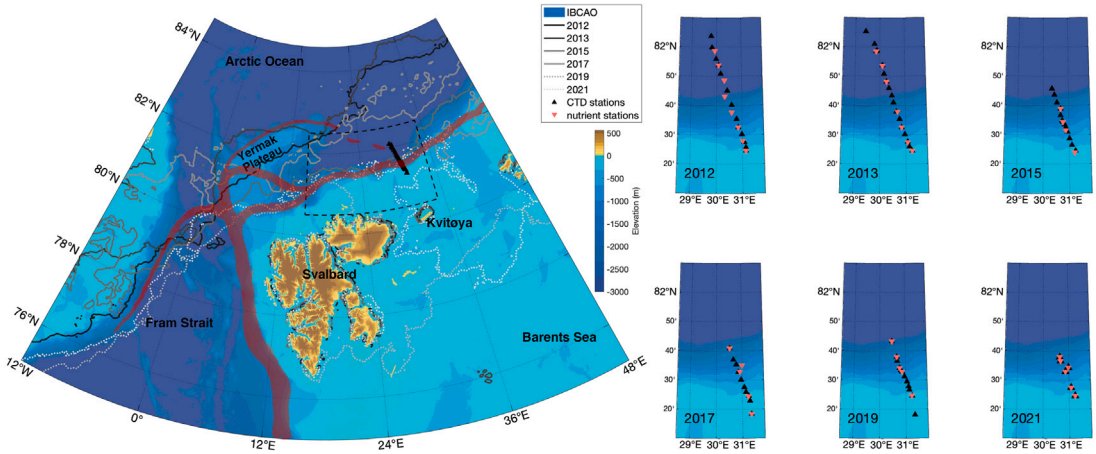

Fig. 1. Left: Large-scale map of the study region. Grey-scale lines (black to white) indicate ice edge position on 15. Sep for 2012–2017 and on 10. Nov for 2019 and 2021. The red broad lines indicate AW pathways including the AW inflow along the shelf break north of Svalbard. Black triangles show CTD station positions of all years. The black, dashed box indicates the area used for sea ice and satellite chlorophyll *a* time series. Background shading indicates bathymetry (IBCAO v.3; Jakobsson et al., 2012) with light/dark blue colours showing shallow/deep regions. Right: Zoom into the transect region with markers showing positions of CTD profiles (black triangles) and nutrient and chlorophyll *a* sampling (red stars) for each year.

a rise in Arctic-wide marine productivity by over 50% since 1998 from measurements of surface chlorophyll *a* (chl *a*) concentrations (Kahru et al., 2016; Lewis et al., 2020). As these satellite measurements do not capture under-ice blooms or chl *a* below the surface, both sea ice and pelagic primary production has, however, likely been underestimated and trend estimates include substantial uncertainty (Ardyna et al., 2020; Ardyna and Arrigo, 2020; Lannuzel et al., 2020).

However, increased productivity requires nutrients, and resupply of nutrients to the euphotic zone is highly dependent on advection, stratification and vertical mixing. There is high uncertainty regarding the future development of the Arctic halocline, the main barrier for nutrient transfer from below into the surface mixed layer, with different patterns across the Arctic Ocean (Randelhoff et al., 2020; Muilwijk et al., 2023). While accumulation of freshwater in the Beaufort Gyre has lead to strengthening of stratification and deepening of the halocline, increased advection of heat with Atlantic Water (AW) inflow, shoaling of the AW layer, and loss of sea ice have weakened the halocline in the Eurasian Basin (Polyakov et al., 2017). While this could enable greater vertical nutrient flux to alleviate nutrient limitation (Randelhoff et al., 2018), Polyakov et al. (2020) report a decline in nutrient concentrations in the halocline of the Eurasian Basin, potentially as a result of enhanced biological uptake upstream in the Barents Sea. Even further upstream, a decline in silicate and nitrate has been reported for the North Atlantic and in the Barents Sea (Rey, 2012; Hátún et al., 2017; Tuerena et al., 2022; Gundersen et al., 2022). However this could not be confirmed in the Western Eurasian Basin north of Svalbard where Duarte et al. (2021) found stable concentrations in the AW layer. How climate change will impact drivers of nutrient supply to the euphotic zone in the Arctic Ocean remains an important subject of investigation.

Changes in open water fraction and a more mobile and thinner sea ice cover will alter momentum transfer from the atmosphere to the ocean, potentially increasing or decreasing wind-driven surface ocean stress depending on sea ice concentration, internal stress and roughness (Rainville et al., 2011; Martin et al., 2014, 2016). The region north of Svalbard is experiencing an increase in annual mean surface stress (Martin et al., 2016), and if this trend continues, the additional wind-driven mixing can help to break down stratification and increase vertical nutrient fluxes (Randelhoff et al., 2020). Different modelling studies showed that this mechanism supports increased productivity along the continental slope in the Eurasian Basin and steers variability in primary and secondary production in the Barents Sea (Slagstad et al., 2015; Sandø et al., 2021). The vertical nutrient fluxes resulting from changed sea ice cover can have a major effect especially in summer and early autumn following earlier melt and later freeze-up. Ardyna et al. (2014) describe changes in Arctic phytoplankton phenology, and the combination of more light due to less or thinner sea ice and weaker stratification supporting increased nutrient supply to the surface might lead to autumn phytoplankton blooms as they are more common in lower latitudes.

The warm and nutrient-rich AW enters the Arctic Ocean through the Barents Sea and along the western and northern continental slope of Svalbard (Beszczynska-Möller et al., 2012; Rudels et al., 2015). In the central and eastern Barents Sea, the AW layer loses substantial amounts of heat, becomes denser and subducts below Polar Surface Water (PSW), and thus is at depth when leaving the region to the north through the St Anna Trough (Rudels et al., 2015). To the west and northwest of Svalbard, AW remains at or near the surface until it meets PSW north of Kvitøya (Pérez-Hernández et al., 2017; Renner et al., 2018). This proximity to the surface keeps the northern Svalbard shelf ice free for large parts of the year, in contrast to the eastern Barents Sea. This ice-free region west and northwest of Svalbard has extended eastward as result of increased warming (Onarheim et al., 2014; Smedsrud et al., 2022). The AW inflow west and north of Svalbard forms a boundary current that follows the continental slope eastward (Pnyushkov et al., 2015), propagating signals of upstream changes into the Central Arctic Ocean and leading to borealisation and Atlantification (Polyakov et al., 2020; Ingvaldsen et al., 2021). The AW boundary current creates an environment north of Svalbard in which advection often dominates over local processes; this applies to physical conditions (e.g., Renner et al., 2018) but also for chemical and biogeochemical properties (Randelhoff et al., 2018; Jones et al., 2021) and transport of biological material and organisms (Wassmann et al., 2015; Vernet et al., 2019; Dybwad et al., 2022). However, larger-scale Arctic Ocean circulation impacts the region by bringing in Arctic sea ice and Polar Surface Waters (Lundesgaard et al., 2021), leading to subduction of the AW layer and transition to more Arctic-like conditions impacting hydrography, nutrient availability, primary production and carbon flux (Henley et al., 2020; Dybwad et al., 2021, 2022).

In this study, we investigate late summer and early winter conditions in hydrography, inorganic nutrients and chl *a* distributions along a transect crossing the Atlantic Water Boundary Current from the shelf to the deep basin north of Svalbard (Fig. 1) over the period 2012–2021. In particular, we look into the connection between sea ice conditions and development of surface chl *a* concentrations during spring and

Table 1
Sampling details of the repeat transects.

Start and end date (period of nutrient sampling)	N–S extent	Bottom depth range	Ship	# CTD/nutrient stations along transect	Depth range sampled
14–27 Sep 2012 (16-25 Sep 2012)	81 24.5 – 82 03.7 N	209-3297 m	RV Lance	13/8	full depth
13 Sep – 01 Oct 2013 (15.–18. Sep 2013)	81 24.5 – 82 05.3 N	202-3354 m	RV Lance	17/8	full depth
13–25 Sep 2015 (14.–19. Sep 2015)	81 24.6 – 81 45.7 N	194-2956 m	RV Lance	13/4	full depth
14-26 Sep 2017 (16.–24. Sep 2017)	81 18.3 – 81 41.0 N	195-2807 m	RV Lance	10/5	0-1000 m
12–27 Nov 2019 (19.–21. Nov 2019)	81 18.1 – 81 43.3 N	184-2921 m	RV Kronprins Haakon	12/5	full depth
06–16 Nov 2021 (09.–11. Nov 2021)	81 24.6 – 81 37.9 N	208–2049 m	RV Kronprins Haakon	6/6	full depth

Table 2
Water mass definitions following Rudels et al. (2000) and Meyer et al. (2017).

warm Polar Surface Water (wPSW)	$T \geq 0$ °C, $\sigma_0 < 27.7$
Polar Surface Water (PSW)	$T < 0$ °C, $\sigma_0 < 27.7$
Modified Atlantic Water (MAW)	$T < 2$ °C, $27.7 \leq \sigma_0 < 27.97$
Atlantic Water (AW)	$T \geq 2$ °C, $27.7 \leq \sigma_0 < 27.97$
deep MAW	$T \geq 0$ °C, $\sigma_0 \geq 27.97$, $\sigma_{0.5} < 30.444$
Intermediate Water (IW)	$T < 0$ °C, $\sigma_0 \geq 27.97$, $\sigma_{0.5} < 30.444$
Deep Water (DW)	$\sigma_{0.5} \geq 30.444$

summer and how they affect hydrography, nutrient availability and chl *a* distribution at the end of summer. By assessing the impact of late summer to autumn wind conditions and the role of sea ice for the interannual variability of these parameters, we evaluate whether a change in sea ice conditions would support the development of autumn blooms and thus a potential increase in primary production in the region.

2. Methods

The transect is primarily a north–south meridional section situated at approximately 31°E, starting at about 200 m water depth on the continental shelf north of Kvitøya and extending north into the Arctic basin to depths of >3000 m (Fig. 1). Repeat measurements along the transect were carried out onboard R/V Lance in September 2012, 2013, 2015 and 2017, and onboard R/V Kronprins Haakon in November 2019 and 2021 during mooring service cruises for the A-TWAIN mooring array (see, e.g., Renner et al., 2018; Lundesgaard et al., 2021). Throughout this study, we refer to September as late summer and to November as early winter to reflect seasonal conditions for phytoplankton productivity in the region. Measurements included vertical profiles of temperature and salinity, and water samples for inorganic nutrients (nitrate, nitrite, phosphate, silicate), chl *a* and phaeophytin (Table 1).

2.1. Hydrography

Temperature and salinity were measured using a Seabird 911+ conductivity–temperature–depth (CTD) sonde. The temperature and conductivity sensors were factory calibrated annually. In 2012, 2019 and 2021, additional calibration of the conductivity sensor was done against in situ salinity samples. The 2012 sampling and processing are described in Våge et al. (2016); no calibration factor was applied. In 2019 and 2021, samples were taken at the bottom of each cast and analysed at the Institute of Marine Research, Bergen, Norway, using a Guildline Portasal salinometer and IAPSO standard seawater. Deviation between conductivity sensor measurements and salinity samples was 0.011 and 0.001 mS/cm for 2019 and 2021, respectively. In 2013, the conductivity sensor was biased low and a correction of $conductivity_{calibrated} = 1.007 \cdot conductivity_{original}$ was applied using deep water properties (Pérez-Hernández et al., 2017). In 2019 and 2021, the CTD was deployed through the ship's moon pool and any data points shallower than 14 m were discarded. For all years, CTD data from the downcast were used for analyses.

The main focus of the cruises was mooring recovery and deployment. This, together with weather and sea ice conditions, caused stations on the transect to occasionally be covered multiple times, not in order by latitude or with time gaps, and the northward extent of the transect varied between years. To construct consistent, near-synoptic (whenever possible) sections for analysis, station data were included depending on alignment with the main transect, concurrent water sampling for nutrients, and shortest possible time difference between casts. In particular, stations that were taken close to but not on the main transect as part of additional transects or in connection with mooring operations (see e.g. station maps in Våge et al., 2016; Pérez-Hernández et al., 2017) were not used here. Single stations with nutrient samples were occasionally not included in the hydrographic section plots and analyses when they disrupted an otherwise near-synoptic coverage of the transect, which mainly was the case when water samples were taken during a repeat station before or after the main transect was covered. CTD data were converted and processed using combination of Seabird Seasoft software and Matlab routines to remove outliers and loops, and binned to 1 dbar bins. We used the GSW Oceanographic Toolbox of TEOS-10 (IOC et al., 2010) to derive conservative temperature T, absolute salinity SA, potential density anomaly σ_θ, and buoyancy frequency N^2 from the CTD profiles. In a stably stratified fluid, N^2 is positive and a higher N^2 indicates stronger stratification. We therefore use the maximum in N^2 as indicator of the depth of the pycnocline and thus the bottom of the mixed layer.

Table 2 shows the water mass definitions that were used, following Rudels et al. (2000) and Meyer et al. (2017). The original definitions were based on potential temperature (θ), practical salinity (S) and potential density anomaly based on θ and S. We applied the previously used limits to conservative temperature, absolute salinity and potential density anomaly. Comparison of the corresponding variables and the resulting water mass distinctions show that differences are small (T: θ +(−0.006–0.012), SA: S+(0.153–0.168), σ_0: $\sigma_{\theta,S,0}$+(0.001–0.0045)), and we consider them negligible for this study.

We divided the transect into "shelf" (shallower than 265 m), "slope" (between 265 and 1800 m), and "deep basin" (deeper than 1800 m) to distinguish between different regions relative to bottom depth. Averages of temperature and salinity (and nutrients, see below) for the different regions or by water mass were calculated using all available data points, regardless of the different transect length in the different years. While coverage over the deep basin varied considerably, properties within water masses and in the deep part of the transect were rather uniform (except for the AW layer). Sensitivity tests with shortened transects for 2012 and 2013 for hydrography and nutrients show that general results do not change, but patterns related to the AW inflow over the shelf and slope are reinforced when deep basin stations are removed.

2.2. Inorganic nutrients: Nitrate + nitrite, phosphate, silicate

Water samples for nutrient analysis were collected from Niskin bottles mounted on the CTD rosette and closed on the upcast at selected stations (Table 1, Fig. 1) at standard depths of 5 (near surface), 10, 20, 30, 50, 75, 100, 150, 200, 300 and 500 m and near bottom with additional samples at 40, 60, 125 and/or 150 m in some years and depending on bottom depth. The uppermost water samples in 2019 and 2021 were taken at 10 m to avoid the impact of the moon pool.

In all years except 2021, subsamples for determination of nitrate, nitrite (here, we use the sum of nitrate and nitrite, henceforth referred to as nitrate), silicic acid (referred to as silicate) and phosphate were collected in acid-washed tubes and frozen at −20 °C for analysis on land after the cruise. Three parallel subsamples from each sample were analysed at UiT by standard seawater methods using a Flow Solution IV analyser from O. I. Analytical, USA. In 2021, samples were collected in 25 mL polyethylene vials, added chloroform (200 μL) and stored at 4 °C until analysis at IMR Bergen. The analysis was done using a spectrophotometric method (Skalar, Netherlands) following the procedure described in detail in Gundersen et al. (2022). In all years, values were calibrated against reference seawater from Ocean Scientific International Ltd., UK. Detection limits were as follows: nitrate: 0.5 μM; nitrite: 0.5 μM; phosphate: 0.06 μM; and silicate: 0.7 μM. In 2013, samples from one station at 81.72°N resulted in anomalously low nitrate and silicate values. A corresponding signal could not be found in hydrography or chl *a* and phaeophytin values; we therefore suspect contamination or analytical error of the nutrient samples and excluded this station from the following analyses.

To determine the depth to which nutrients were depleted in the surface layer, the depth of the nitracline was defined as the shallowest depth at which the vertical gradient in nitrate concentration became larger than 0.1 μM m^{-1}. In 2019, only two stations along the transect had a vertical gradient > 0.1 μM m^{-1} and no nitracline could be determined at the other stations, and for 2021, none of the stations displayed a distinct nitracline.

Nitrate to phosphate (N/P), nitrate to silicate (N/Si) and silicate to nitrate (Si/N) ratios were determined for each cruise and each nutrient sampling station by the slope of the linear regression between nitrate and phosphate, and silicate and nitrate, respectively, for all relevant samples.

2.3. Chlorophyll a and phaeophytin

Samples for chl *a* and phaeopigments were collected for calibration of the CTD-mounted fluorescence sensor as well as to complement nutrient samples for biological conditions. Triplicate samples of 0.2–0.5 L were filtered through 0.7 μm GF/F filters (total chl *a* and phaeopigments) and 10 μm polycarbonate filters (chl *a* and phaeopigments > 10 μm), extracted in 100% methanol for minimum 12 h at 4 °C and in darkness. The samples were analysed onboard, or filters were frozen at −20 °C and analysed in the lab at UiT. After homogenisation, fluorescence was measured before and after acidification with two drops of 5% HCl using a Turner AU-10 fluorometer. Chl *a* and phaeopigment concentrations were calculated based on equations from Holm-Hansen and Riemann (1978). The fluorometer was calibrated using a dilution series of pure chl *a* (analytical standard).

To calibrate the fluorescence sensor mounted on the CTD, fluorescence values were extracted for each profile and depth where a chl *a* sample was taken. A linear regression model was then derived by fitting the extracted fluorescence to the corresponding measured chl *a* concentration (regression statistically significant at $p < 0.005$ in all years) and used to calibrate the CTD fluorescence profiles. For 2021, no chl *a* concentration data from seawater samples were available from our cruise or the cruises right before or after using the same fluorometer. However, CTD fluorescence was very low and near the noise level of the sensor, indicating very low winter chl *a* concentrations, and we would not expect any significant changes from calibration against water samples.

2.4. Satellite and reanalysis data

Daily sea ice concentration data derived from AMSR-2 was downloaded from the Institute of Environmental Physics, University of Bremen, Germany (Spreen et al., 2008), available at https://seaice.uni-bremen.de/sea-ice-concentration-amsr-eamsr2/. Daily, satellite-sensed, near-surface chlorophyll *a* (chl_{sat}) concentration was derived from open access MODIS Aqua data products (Level 3 Standard Mapped Image (SMI), chlorophyll *a*, 9 km resolution; NASA Goddard Space Flight Center, 2022), obtained from http://oceandata.sci.gsfc.nasa.gov, accessed on 01.07.2019 for 2012–2017 data and on 01.06.2022 for 2018–2021. To distinguish between chl *a* from water samples, CTD fluorescence and satellite, we will refer to them as chl *a*, chl_{CTD} and chl_{sat}, respectively, throughout the manuscript.

To examine the temporal development of the sea ice cover and chl_{sat} concentrations in the region of our transect, we defined an area covering the latitudinal extent of the transect and including the upstream region with the boundaries 80.5–82.5°N, 15–35°E to calculate daily averages. This area allows for sufficient satellite data coverage for chl_{sat} even in periods with sea ice cover while avoiding inclusion of signals due to different circulation patterns further west. See Figure S1 for spatial distribution of data availability per year. Sensitivity test with different box sizes (not shown) confirm that results are stable and do not change significantly with smaller or larger boxes (while still avoiding reaching into the Fram Strait outflow). However, in years with extensive ice cover throughout the summer and thus limited satellite observation, the chl_{sat} time series likely underestimates surface chlorophyll concentrations. From approximately mid-September to mid-March, low sun elevation angle and/or lack of sunlight prevent chl_{sat} measurements in our study region, restricting possible detection of surface chlorophyll during autumn.

Hourly data for surface wind, air temperature, net shortwave and longwave radiation and surface humidity from ERA5 reanalysis were accessed and downloaded from the Copernicus Climate Change Service Climate Data Store on 25 and 27 July 2023 (Hersbach et al., 2023a,b).

3. Results

3.1. Hydrography

The temperature and salinity transects at 31°E in both September (2012, 2013, 2015, and 2017) and November (2019 and 2021) reflect the general structure across the Atlantic Water Boundary Current from the shelf to the deep basin north of Svalbard with a fresh surface layer above AW and intermediate and deep water masses (Pérez-Hernández et al., 2017; Våge et al., 2016; Figs. 2, 3, S2). The characteristics of the surface layer vary between years and along the transect. On average, the surface layer (PSW and warm PSW), defined as the layer with $\sigma_0 < 27.7$ (Table 2), is fresher (<35 g kg^{-1}) and colder (<3 °C) than the underlying AW. Using the definition in Table 2, there often is a transition layer from surface waters to AW, where heat loss and interaction between the water masses creates cooler and slightly fresher modified AW (MAW). The dominant AW with high T (2–5 °C) and high SA (>34.9 g kg^{-1}) extends from <50 m to the bottom over the shelf and upper continental slope, i.e. the core of the AW inflow, and from > 50 m to approximately 500 to 600 m in the deeper parts of the transect. The warmest water in the AW layer is generally located above the slope with $T > 4$ °C in both late summer (2012–2017) and early winter (2019 and 2021). In late summer, maximum salinity is >35.21 g kg^{-1}, whereas in early winter, SA reaches only 35.15 g kg^{-1}. Below the AW layer, there is a transition layer (deep MAW) to Intermediate Water (IW), which is considerably colder than AW, and then Deep Water (DW). Note that in 2017, no Deep Water was captured as CTD casts did not extend deep enough (Fig. 3). Average hydrographic properties of each water mass by year are given in Table S1. For this study, we will focus on the water layers from AW upwards.

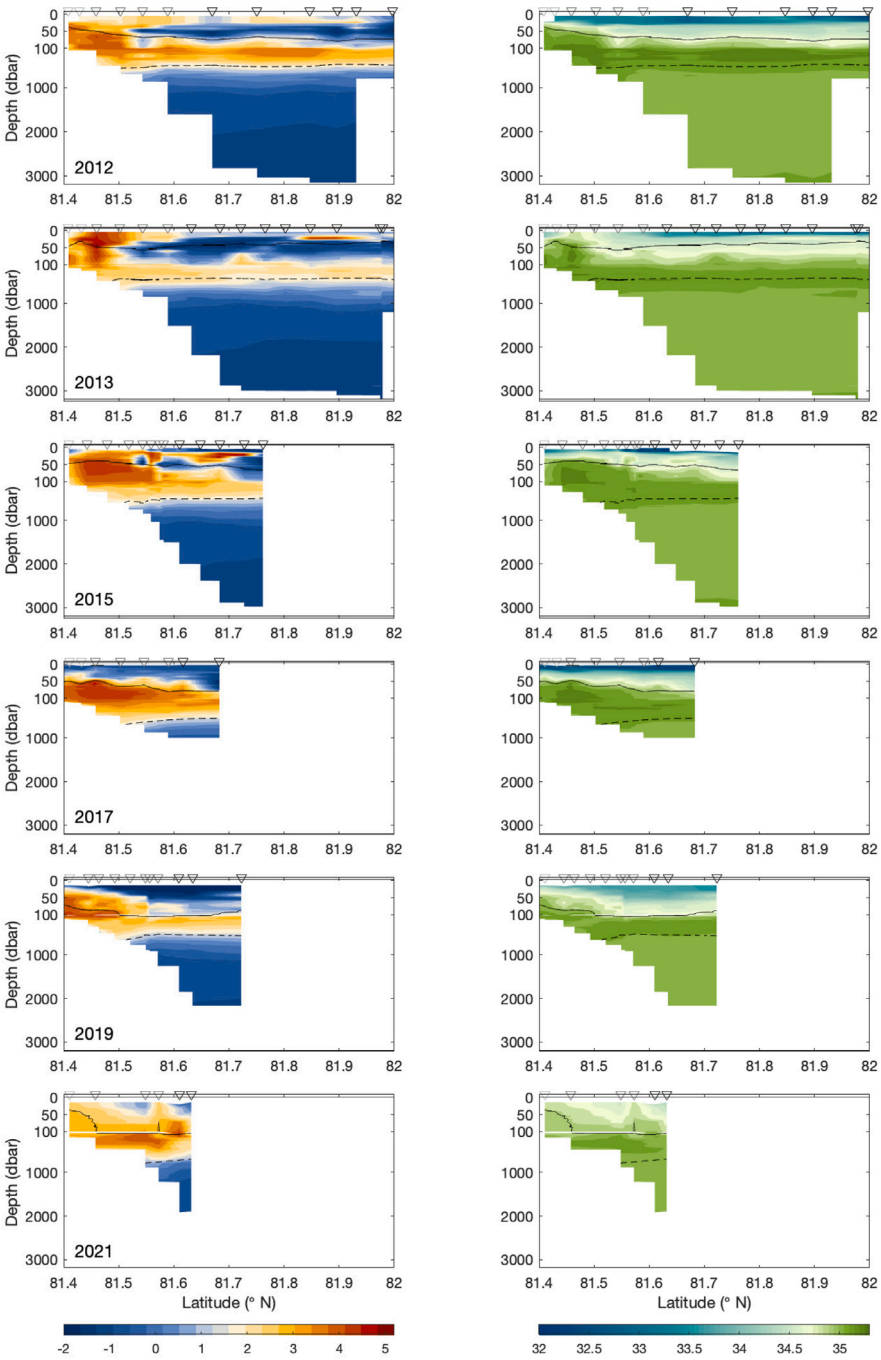

Fig. 2. Left: Conservative temperature (°C). Right: Absolute Salinity (g kg^{-1}). Solid black line indicates the $\sigma_0 = 27.7$ isopycnal, dashed black line shows the $\sigma_0 = 27.97$ isopycnal. Triangles on top indicate positions of CTD stations along the transect by depth: light grey = shelf, dark grey = slope, black = deep stations. Note the change in resolution on the y-axis at 100 m depth.

There is considerable interannual variability in the surface and AW layer properties. In 2012, warm PSW (wPSW) extended over almost the entire transect to approximately 81.95°N, and reaching 25 m depth furthest north and ~50 m on the shelf and upper slope. Below that, PSW was present from the deeper part of the slope northwards and down to a depth of approx. 70 m. AW occupied between 400 to 350 m of the water column from shelf/slope to the deep basin with the warmest AW located above the upper slope (maximum $T = 4.1$ °C). In 2013, wPSW was also present over the entire transect but with lower temperatures than in 2012 over the deeper part, and with strong influence of AW over the shelf and slope with high temperatures (up to 4.6 °C) and salinities (34.87 g kg^{-1}) reaching all the way to the surface. A colder, saltier and deeper (to around 200 m) PSW is connected to an anomalously cold AW layer in 2013 where temperatures rarely reached more than 2.5 °C in the deeper part of the transect. Due to the generally lower temperatures, less of the water column was occupied by AW and a larger part by MAW, both above and below the AW layer, than in 2012. In 2015, warm water reached to the surface above the slope similar to 2013, although with distinctly lower salinities. At the shallowest shelf station, the warm layer was capped off by colder and fresher surface water. In the deep part of the transect, PSW extended to similar depth as in 2012 but is colder and fresher at the surface (T near freezing point, $SA < 31.5$ g kg^{-1}). The AW has similar properties above the slope as in 2012, but becomes fresher and colder in the deep basin and occupies a thinner layer (120–430 m depth at the northernmost end of the transect). 2017 stands out with different conditions in the surface

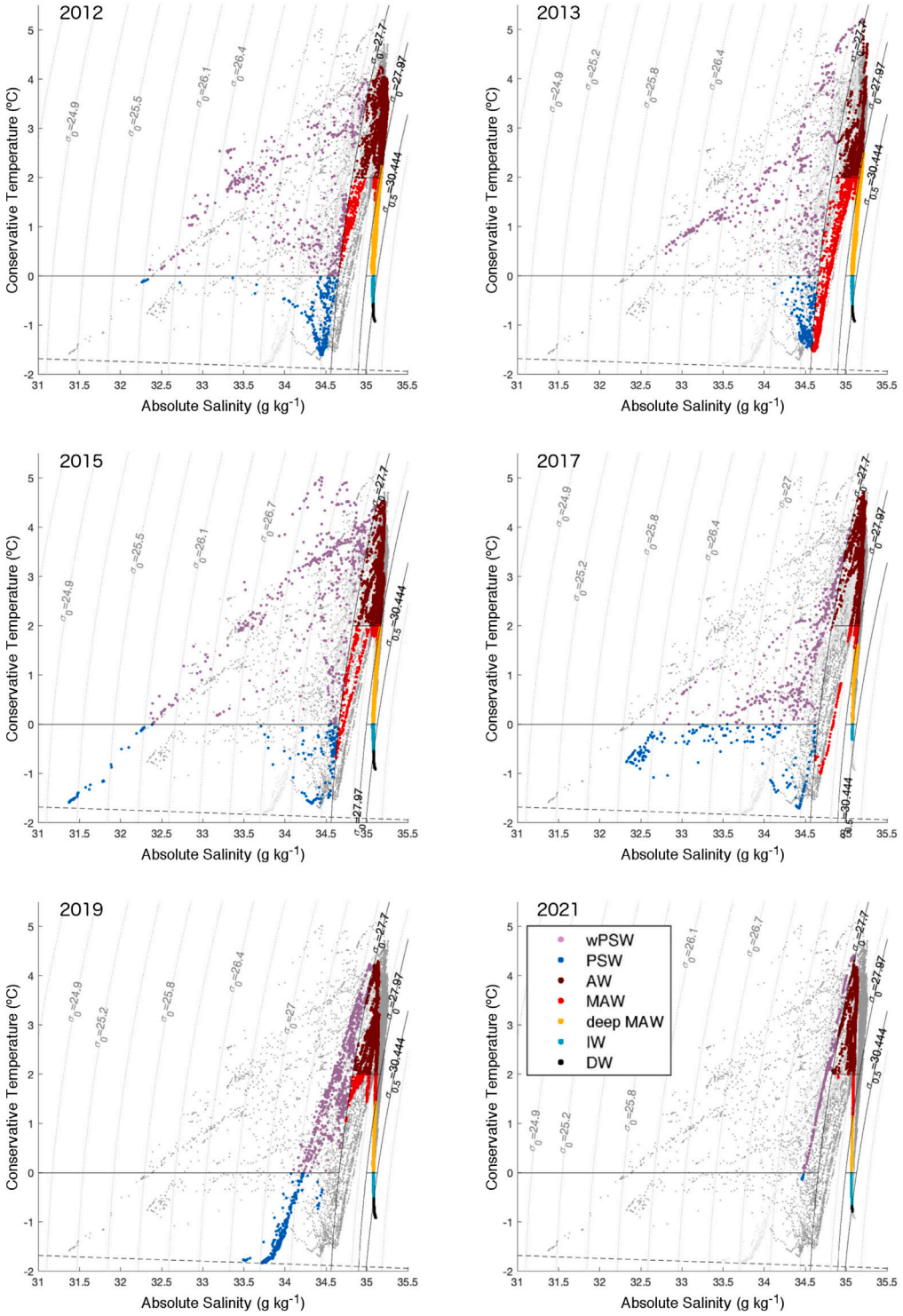

Fig. 3. T–SA diagrams for each year colour-coded by water mass. Data from all years combined is shown as grey dots (dark grey = late summer, light grey = early winter data). Grey solid lines indicate boundaries for water mass definition. The grey dashed line indicates the freezing temperature.

layer compared to the previous years. Over the entire transect including the shelf and slope, a cold and fresh PSW layer separated the AW from the surface and no wPSW was present. The AW layer was warmer than in 2012–2015 and in the deep basin occupied a similar depth range as in 2012 (80–500 m depth). In 2017, AW salinities on the upper slope were higher than in 2012–2015 with $SA_{slope} = 35.17$ g kg^{-1}.

Interannual variability in early winter conditions was similarly large as in late summer. The two transects conducted in November 2019 and 2021 show very different patterns both in surface layer properties and AW properties. 2019 was characterised by a very cold (surface temperatures at freezing point over most of the transect) but saline surface layer compared to late summer conditions ($SA > 34.5$ g kg^{-1}). The core of the AW inflow, characterised by high temperatures and salinities (and a maximum in current velocities in the AW layer; Pérez-Hernández et al., 2017) over the shelf and upper slope was warm compared to the late summer transects in 2012–2017 and the early winter transect of 2021 whereas the AW layer towards the deeper part of the transect was rather cold. The AW salinity was lower than

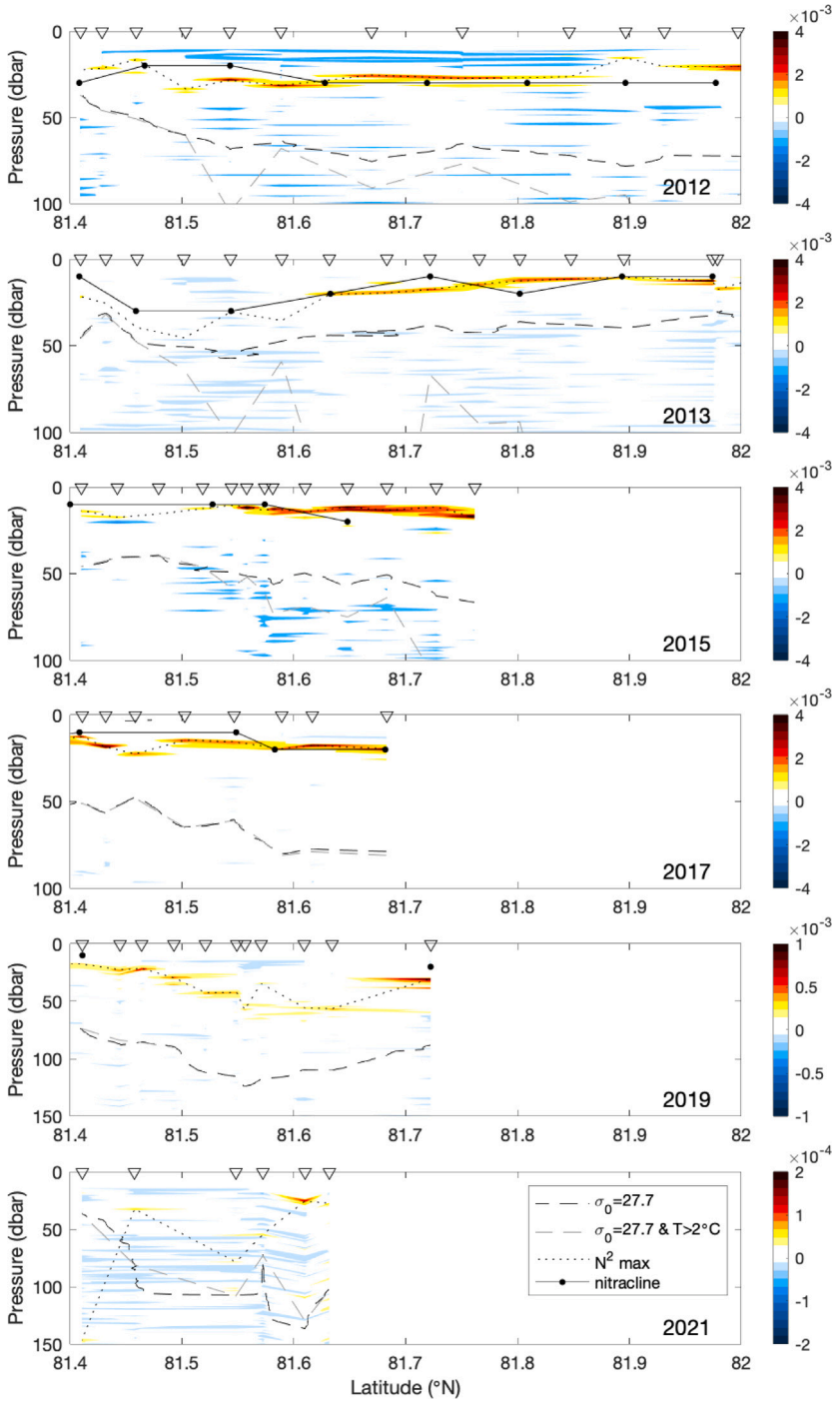

Fig. 4. Buoyancy frequency N^2 (s^{-2}) in the upper 100 m (150 m for 2019 and 2021) across the transects. Black dotted lines show the depth of N^2 maximum (corresponding to the bottom depth of the surface mixed layer); black dashed lines indicate the σ_0 = 27.7 isopycnal; grey dashed lines indicate the depth with σ_0 > 27.7 and T > 2 °C; black lines with symbols show the nitracline from water samples. Please note the change in colour scale for 2019 and 2021, necessitated by weaker N^2 in these transects and order of magnitude difference between the two years.

in the late summer transects. The dip in temperature and salinity at approximately 81.55°N in Fig. 2 is due to non-synoptic coverage of the transect, i.e., an extended time gap between two adjacent stations in 2019 that could have allowed for, e.g., a reversal in tidal currents. In 2021, transect coverage into the deep basin was limited. However, the AW layer extends to the surface along most of the transect, and the surface layer resembles more modified AW than wPSW due to its high salinity (Figs. 2, 3). Only small pockets of slightly colder and fresher SW with T reaching 0 °C and minimum SA at 34.46 g kg^{-1} exist over the deeper part of the transect. The AW core appears to be situated both deeper in the water column and further north above greater water depth than in November 2019 and than in any of the September transects. T and SA in the AW layer in 2021 are comparable to 2019, i.e. overall similar temperatures as in the other years, but slightly lower salinity.

The differences in hydrography between years and seasons is also reflected in the strength of stratification, expressed here by the buoyancy frequency N^2 (Fig. 4). In general, maximum N^2 is higher and shallower in the late summer transects (2012–2017) than in early winter (2019 and 2021). The transects extending furthest north (2012

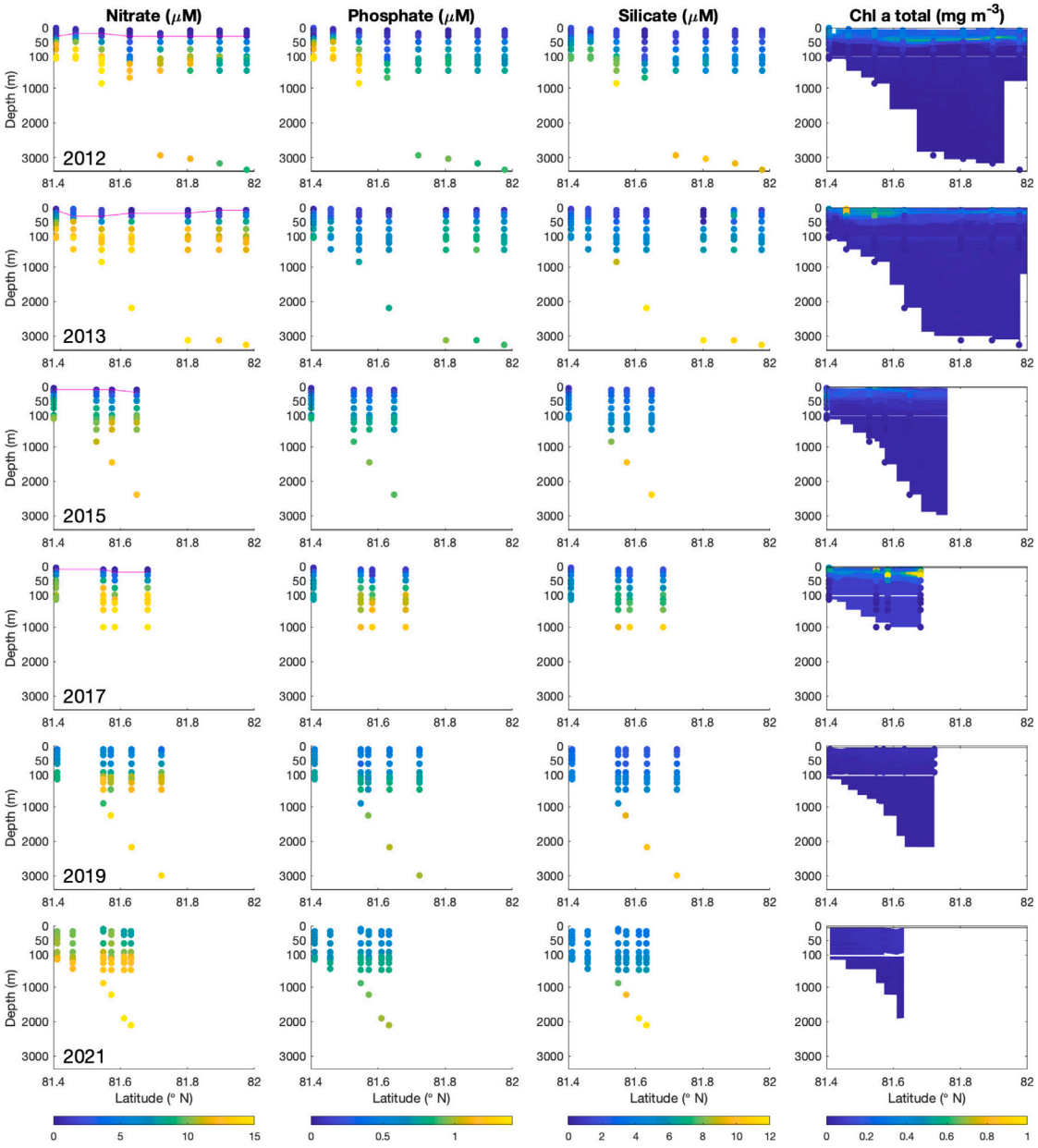

Fig. 5. Left to right: Full depth nitrate (μM), phosphate (μM), silicate (μM) and chl *a* (mg m^{-3}) concentrations along the transect in 2012–2021. Magenta lines indicate the nitracline defined as the depth at which the gradient in nitrate concentration was >0.1 μM m^{-1}. Chl *a* from both CTD fluorescence (chl_{CTD}; background colour) and bottle samples (coloured circles; not available for 2021) are presented. Please note the change in resolution on the *y*-axis at 100 m depth. A zoom into the upper 150 m of the nutrient data is shown in Figure S3.

and 2013) experience low maximum N^2 over the shelf and upper slope, suggesting weak stratification, and shoaling of the maximum N^2 from the deeper part of the slope to the deep basin. Strongest late summer stratification is observed in 2015, located highest in the water column, closely followed by 2017 when N^2 was high above the shelf and slope due to the extensive PSW layer. The early winter transect in 2019 shows a clear N^2 maximum throughout the transect, though weaker and shallower than in the late summer transects, whereas in 2021, N^2 is low throughout the water column above the shelf and slope and only reaches a clearer maximum at the deepest stations.

3.2. Nutrient distributions

In general, nitrate, phosphate and silicate concentrations in late summer (2012–2017) were low in the surface layer, increasing with depth to around 75–100 m, below which concentrations remained stably high (Fig. 5, Table S2). Nitrate and phosphate were low at the surface ($[NO_3]$ < 2 μM, $[PO_4]$ < 0.25 μM to 20 m depth) in all late summer transects, whereas surface silicate concentrations were more variable (0.8–2.5 μM in the upper 20 m). Along the transect, highest concentrations of all nutrients occurred in the near-bottom samples over the continental slope and in the deep basin (maximum $[NO_3]$, $[PO_4]$, and $[SiOH_4]$ of >12.96, 0.95 and 10.5 μM, respectively, across all years and stations). The long transects in 2012 and 2013 indicate that nitrate concentrations throughout the water column decreased with latitude. The early winter transects in 2019 and 2021 show two very different scenarios, but in both years, surface nutrient concentrations were considerably higher than in the late summer years whereas concentrations below the mixed layer were comparable (Table S2).

As with the hydrography, nutrient concentrations varied between years, both in absolute numbers and distribution (Figs. 5, 6, S3). In 2012, we observed the deepest nitracline of all years at around 30 m

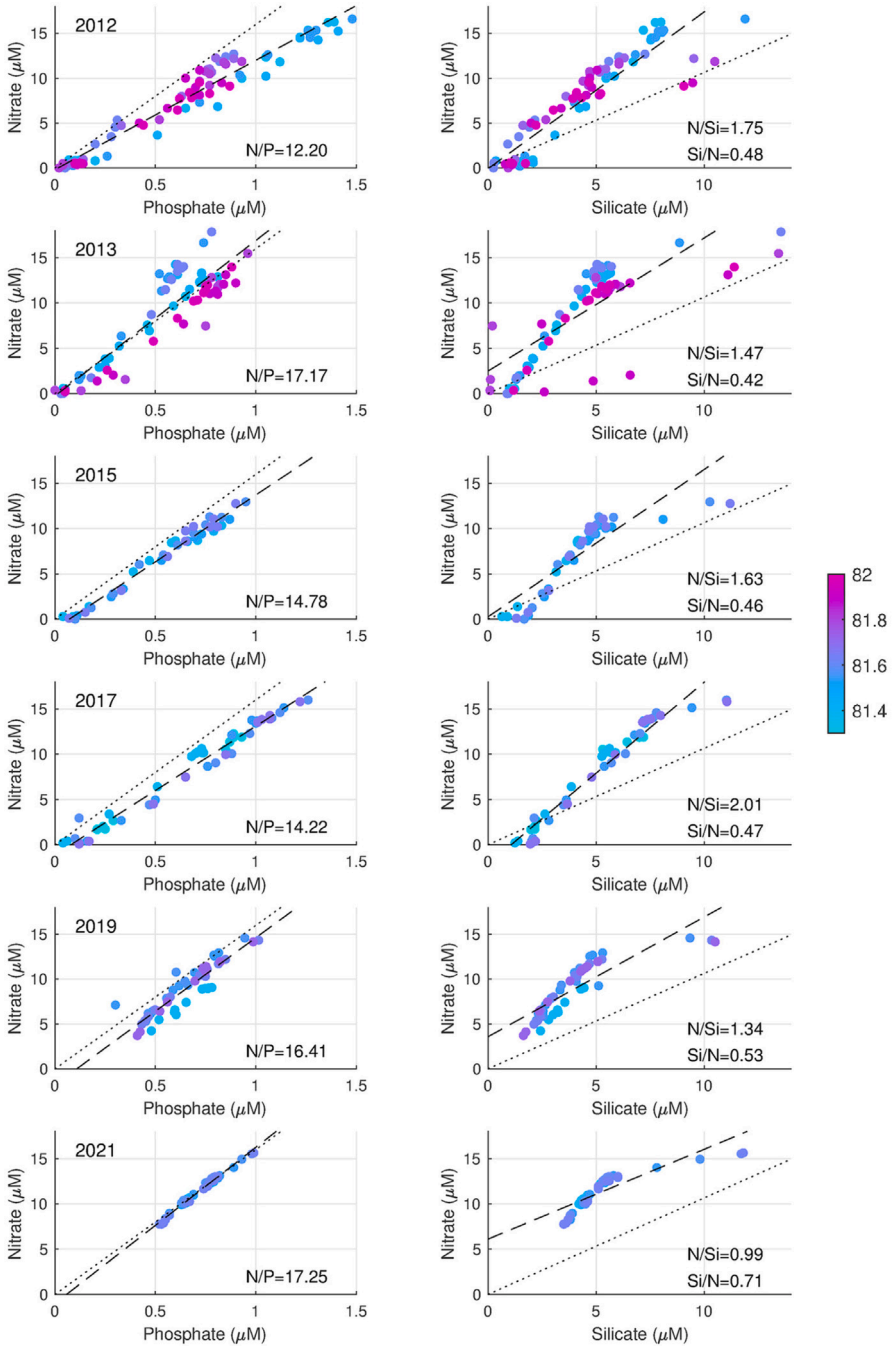

Fig. 6. Nitrate (μM) versus phosphate (μM) (left) and versus silicate (μM) (right). Colour indicates latitude (°N). Ratios are given as slope of the linear regression between phosphate and nitrate and nitrate and silicate, respectively. Both N/Si and Si/N ratios are shown for easier comparison with literature. The dotted lines indicate the idealised Redfield ratios (N/P = 16/1, N/Si = 16/15); the dashed lines show the results of the linear regressions.

(Fig. 5). Nitrate concentrations above the nitracline were very low in 2012 ([NO_3] < 0.84 μM), particularly over the slope and deep basin. However, at the nitracline and directly below, concentrations were high, especially over the slope, which might be related to the strong signal of the AW inflow. The N/P ratio over the shelf and slope was lowest for all years in 2012 while the Si/N ratio was comparatively high; both likely due to the very low surface nitrate concentrations, and the elevated phosphate and silicate concentrations below the nitracline (Fig. 6). In 2013, the nitracline was generally shallower than in 2012 but also more variable along the transect. Nitrate concentrations were considerably higher above the nitracline along the entire transect and below the nitracline over the slope and the deep basin. While the AW inflow promoted a local temperature maximum and elevated salinity reaching to the surface over the slope (Fig. 2), this was not reflected in higher phosphate concentrations there, and only partially so for silicate concentrations. On the contrary, phosphate concentrations in AW-influenced layers were lower over the shelf and slope than in the deep basin. The resulting overall N/P ratios were higher in 2013 than in 2012 whereas Si/N was lower (Fig. 6). However, looking in more detail at the ratios by latitude, especially the N/P ratios vary considerably along the transect, with high ratios over the shelf and slope and lower N/P ratios in the deep basin.

The nutrient transect in 2015 was the shortest of late summer transects. It crosses the core of the AW inflow but provides only limited information in the deep basin. Nutrient concentrations and nitracline depth are less variable than in the previous years. None of the nutrient

distributions reflect the signal of the AW inflow over the slope. Instead, concentrations are evenly distributed along the entire transect and low at depth compared to the other late summer measurements. In 2017, both nutrient concentrations and distributions were similar again to 2012 and 2013, with low concentrations in the surface layer and high values at depth. The nitracline was rather shallow, particularly over the shelf, and the surface layer was not as clearly depleted as in 2012 and 2013. The highest concentrations are observed at depth over the deeper part of the slope and the deep basin instead of in the AW inflow core, which is in contrast to 2012 and 2013. N/P ratios are rather low and on similar levels as in 2015, whereas the Si/N ratios are among the highest of all years due to the relatively high silicate concentrations throughout the water column. Si/N uptake ratios around 0.5 by late summer might indicate nitrate uptake by the non-silicate haptophyte *Phaeocystis pouchetii* (Assmy et al., 2017; Henley et al., 2020) after which silicate uptake can occur as diatom blooms develop during the seasonal transitions as found in the Barents Sea (Jones et al., 2023; Koenig et al., 2023).

The winter transects in 2019 and 2021 differ from the late summer transect in 2012–2017 most clearly in the surface mixed layer nutrient concentrations (Figs. 5, S3, Table S2). In 2019, this surface layer was still fairly pronounced with low nutrient concentrations, but replenishment had started and nitrate and phosphate concentrations in the PSW and wPSW were >5.6 μM and >0.5 μM, respectively. Near-surface silicate concentrations, however, were higher in 2017. The vertical gradient in nitrate concentration was eroded to the point that a nitracline according to the definition outlined in Section 2.2 could only be determined at two stations (the one furthest south and furthest north, with 10 and 20 m, respectively). Below the surface mixed layer, concentrations were on similar levels as the previous years, and a clear signal of the AW inflow was lacking in the latitudinal nutrient distributions despite the presence of an AW inflow signature in the hydrographic properties (Fig. 2). Although sampled slightly earlier in November, the 2021 surface nutrient concentrations (PSW and wPSW) were even higher, and the vertical gradient was eroded further than in 2019. Concentrations at depth are comparable to the previous early winter transect in 2019. The only exceptions were nitrate concentrations on the shelf and upper slope that were higher than in 2019. Si/N was markedly higher in 2021 compared to 2019. This increase indicates that an additional source might have contributed silicate to the water column north of Svalbard.

3.3. Chl *a* and phaeophytin distributions

In all late summer transects, chl *a* was primarily found in the surface layer above 50 m (Figs. 5, 7 and S4). Below that, both bottle and CTD fluorescence data showed little to no chl *a*. Patterns were similar for total and size-fractionated (>10 μm) chl *a* and phaeophytin concentrations. Size-fractionated chl *a* indicated higher fractions of larger phytoplankton cells below the mixed layer in most years. Phaeophytin is the degraded product of chl *a*, and the ratio $[phaeophytin]/[phaeophytin + chl\ a]$ indicates how fresh the algal material is, with a higher phaeophytin to chl *a* ratio indicating a higher degree of degradation (e.g., Yentsch, 1965; Gaffey et al., 2022, and references therein). Degradation can result from microbial degradation or zooplankton grazing. Total phaeophytin to chl *a* ratios were generally lower in the mixed layer and elevated below, whereas the size-fractionated phaeophytin to chl *a* ratios (not shown) were more variable, both between years and along the transect.

In 2012, chl_{CTD} indicated a deep chl *a* maximum with highest concentrations at the bottom of the pycnocline. In the bottle samples this pattern is not quite as clear with more even distribution of chl *a* reaching up to 0.43 mg m^{-3} throughout the surface mixed layer and along the transect, possibly because of the bottle sample depths not matching the depths of the deep chl *a* maximum. Surface size-fractionated chl *a* (>10 μm) was elevated above the shelf and slope relative to the deep basin. Ratios between size-fractionated chl *a* and total chl *a* indicate a higher fraction of large phytoplankton below the mixed layer and in the deep basin. Total phaeophytin concentrations are higher over shelf and slope than over the deep basin, whereas the pattern is opposite for size-fractionated phaeophytin (>10 μm). Phaeophytin to chl *a* ratios are higher below the mixed layer for total concentrations, but not for the >10 μm size fraction. In 2013, chl *a* concentrations were second highest after those concentrations in 2017 with a marked maximum from the surface to the bottom of the mixed layer above the shelf and upper slope (up to 0.85 mg m^{-3}). This maximum was also present in total phaeophytin, and size-fractionated chl *a* and phaeophytin. In contrast to 2012, most of the chl *a* was confined to the layer above the pycnocline, and only in the deeper part of the transect, a deep chl *a* maximum had formed at the bottom of the pycnocline.

2015 stood out with the lowest chl *a* concentrations of the four years of late summer observations (<0.28 mg m^{-3}) and low size-fractionated chl *a* off the shelf. Total phaeophytin concentrations, however, were comparable to 2012, and size-fractionated phaeophytin to chl *a* ratios were the highest of all years, especially below the mixed layer. The phaeophytin to chl *a* ratio was clearly elevated above the shelf and decreased towards the north, similarly to the distribution observed in 2017, when this pattern extend also below the pycnocline. In 2017, the highest concentrations of total and size-fractionated chl *a* and phaeophytin of all years were measured. Chl *a* showed a local maximum over the slope at the bottom of the mixed layer. For the other variables, concentrations were high throughout the surface mixed layer. Ratios of size-fractionated chl *a* and phaeophytin (total and size-fractionated) were elevated compared to the other years.

As expected, chl_{CTD} in the early winter transects 2019 and 2021 (Figs. 5, 7) was low, indicating that there were very low concentrations of chl *a* in the water column in November. Water samples in 2019 showed low concentrations of phaeophytin and chl *a*, and a high phaeophytin to chl *a* ratio, suggesting a high degree of degradation and little fresh algal material. Lack of sunlight prohibits local primary production at this time of year, and the degraded material might have been advected into the region with the AW inflow.

4. Discussion

The transects showed large interannual variability, both in late summer and early winter, and patterns differed for the different parameters. In 2012 and 2013, the hydrographic structure was similar with wPSW at the surface above cold PSW and warm MAW and AW, but nutrient and chl *a* concentrations and distribution varied with low surface-layer nutrient concentrations and a pronounced deep chl *a* maximum in 2012 compared to a shallower, more variable nitracline, highly variable nutrient ratios along the transect and higher surface chl *a* above shelf and slope in 2013. The late summers in 2015 and 2017 were characterised by cold PSW at the surface and a shallow mixed layer, however, in 2015 a sub-surface layer of wPSW was present whereas in 2017, this layer was absent. Nutrient concentrations in the surface layers were similar in both years, but deep concentrations differed considerably with 2017 being more similar to 2012 and 2013. The greatest differences existed, however, in the chl *a* distributions where values were very low in 2015 and high in the pycnocline in 2017. The early winter years 2019 and 2021 were very different in all parameters apart from the very low chl_{CTD} throughout the water column. 2019 was characterised by the presence of a pronounced cold and fresh surface layer with low nutrient concentrations, whereas stratification was weak in 2021 and warm, nutrient-rich AW extended to the surface.

In the following sections, we will discuss potential drivers for the observed differences between the years, in particular the effect of wind-driven mixing and its dependence on the underlying hydrography, and the role of sea ice in shaping upper ocean conditions and chlorophyll distribution at the surface and in the water column. Finally, we speculate on implications of our results for potential future development of autumn blooms in the study region north of Svalbard.

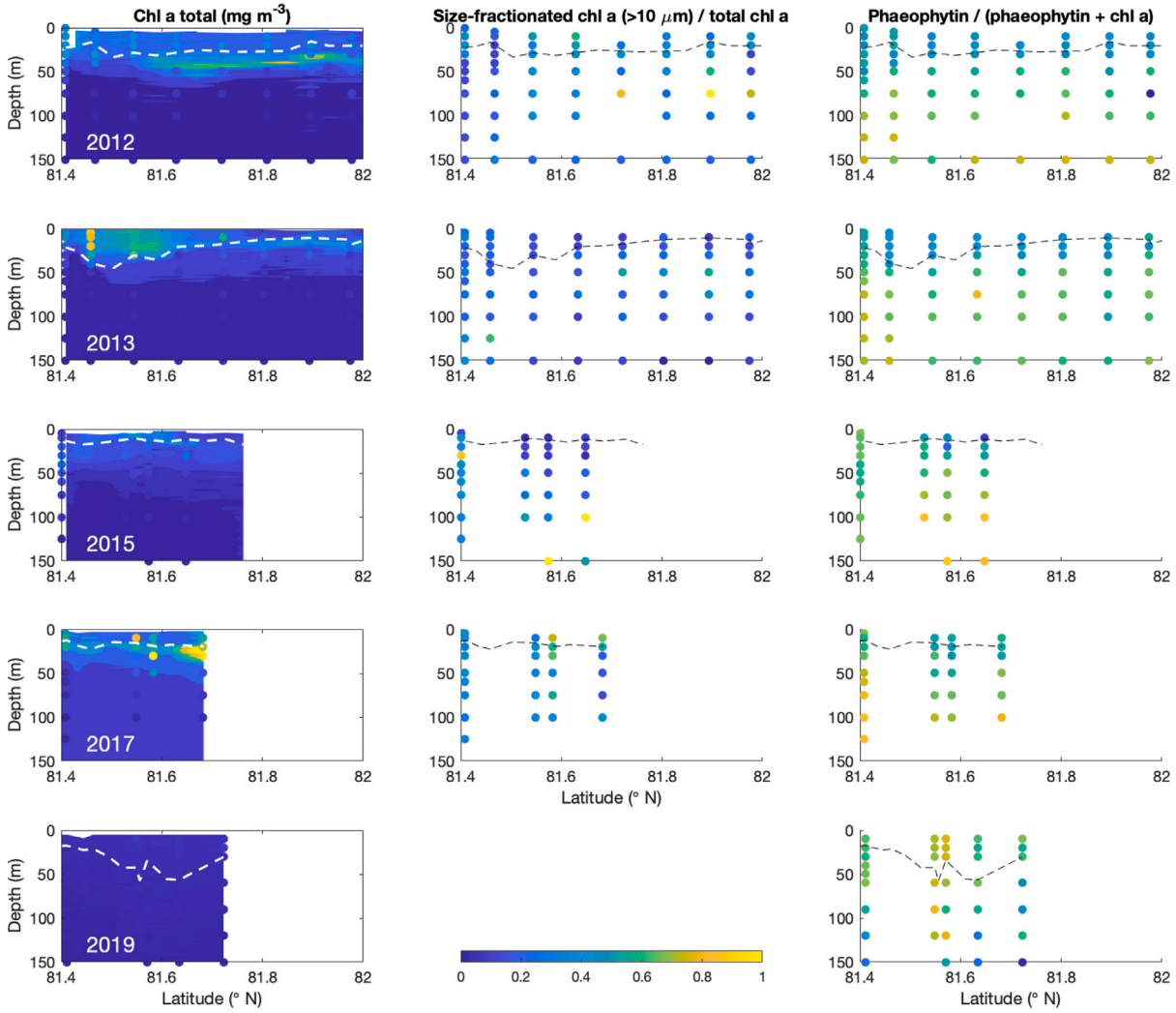

Fig. 7. From left to right: Chl *a* concentrations (mg m^{-3}) in the upper 150 m from bottle samples (coloured circles) and CTD fluorescence (chl_{CTD}; background colour); size fraction for chl *a* > 10 µm (not available for 2019); and phaeophytin to total chl *a* + phaeophytin ratio for 2012, 2013, 2015, 2017 and 2019 (top to bottom). White and black dashed lines indicate mixed layer depth defined by depth of maximum N^2.

4.1. Interannual variability and potential for wind-driven mixing in autumn

The different late summer conditions provide different starting points for breakdown of stratification during autumn and upward mixing of nutrients; the early winter transects reflect the results of this autumn mixing. We tested the potential impact of wind in driving this process in our survey years by calculating the theoretical Ekman depth D_E as indicator for how deep wind-driven mixing could reach (in the absence of strong stratification):

$$D_E = \frac{\pi \rho_a C_d}{\sqrt{2}\rho_W \Omega \alpha} \frac{1}{\sqrt{sin(\theta)}} W \quad (1)$$

with ρ_a = density of air (1.3 g m^{-3}), C_d = drag coefficient (taken as 1.4×10^{-4}), ρ_W = density of water (1026 g m^{-3}), Ω = rotation rate of the Earth, θ = latitude (81.5°N), α = empirical constant (0.0127) and W = wind speed; see, e.g., Peralta-Ferriz and Woodgate (2015). While the theoretical Ekman depth does not equate to the actual wind-driven mixing depth, especially in the presence of sea ice (see, e.g., Cole et al., 2017), it is easier to relate to the mixed layer depth than wind speed itself. Additionally, we apply the one-dimensional bulk mixed layer Price–Weller–Pinkel model (PWP; Price et al., 1986) with modifications to allow for impact of sea ice. A detailed description of the modified model is given in Biddle et al. (2017) and Lagnevall (2017). We used hourly ERA5 reanalysis data (Hersbach et al., 2023a,b) for the period 15 September to 1 December for each of the years that we have hydrographic observations for, as forcing data. Two experiments were run to investigate 1. the impact of each year's wind field and atmospheric conditions on the respective water column structure (years with late summer hydrography measurements only; initiated from the CTD profile in the AW inflow core, roughly above the 800 m isobath, taken in the respective year); and 2. the impact of each year's wind field on the same hydrography (all years; initiated from the 2017 CTD profile in the AW inflow core). Wind conditions, theoretical Ekman depth, and model results (modelled mixed layer depth and N^2) are shown in Fig. 8.

Wind direction and speed from late summer to early winter were highly variable between years. While for example southerly winds with moderate wind speed dominated in 2012, 2021 experienced stronger northerly winds. The theoretical Ekman depth is only depending on the wind speed, and years with higher wind speeds (2013, 2017, 2021) displayed greater Ekman depths than years with low wind speeds (2012, 2015, 2019). If we consider a great Ekman depth to be an indicator for a larger potential for wind-driven mixing and thus greater deepening of the mixed layer, especially the difference between the early winter years corresponds well with the observed differences in mixed layer depth and strength of stratification in 2019 and 2021, where 2021 was considerably weaker stratified (Fig. 4). The results from the modified PWP confirm this pattern: when initiated from the same hydrographic profile, wind and atmospheric conditions in 2021

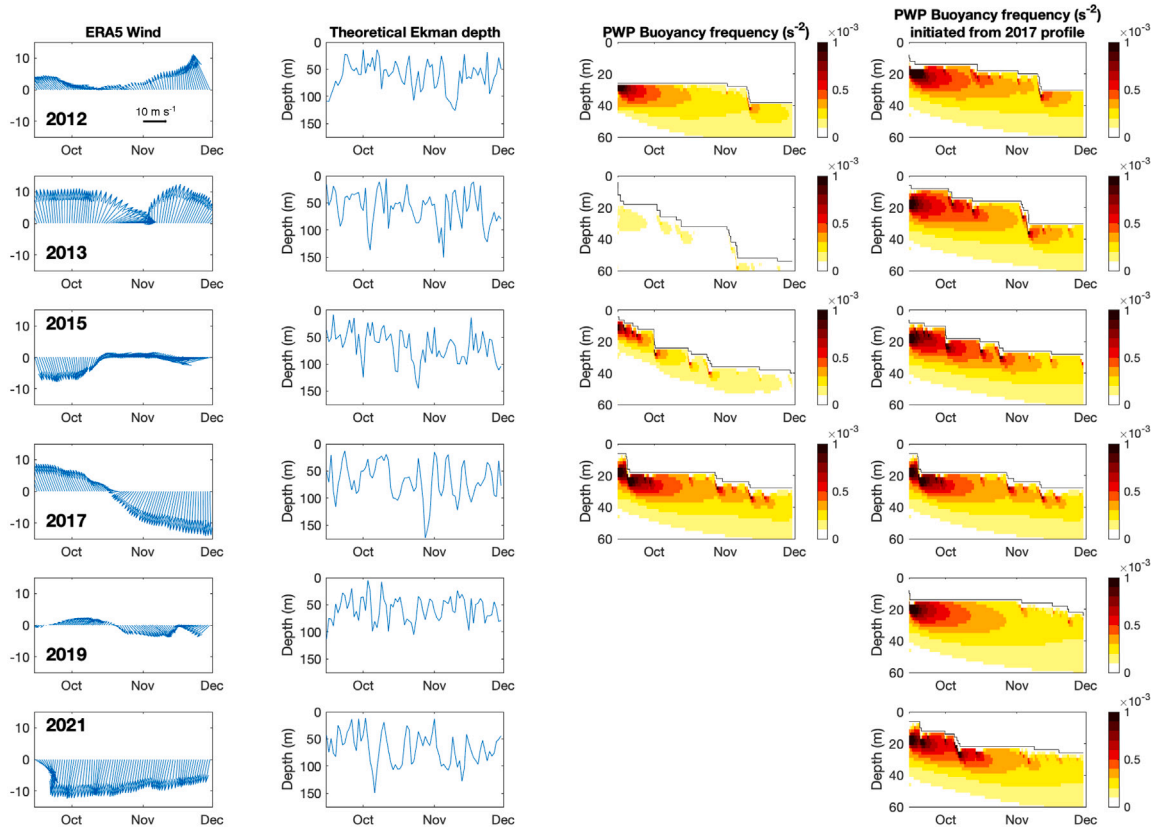

Fig. 8. From left to right: Wind conditions between 15 September and 1 December for each year from ERA5, resulting theoretical daily Ekman Depth, modelled buoyancy frequency and mixed layer depth (black line) in the AW inflow core, and modelled buoyancy frequency and mixed layer depth (black line) starting from 2017 CTD profile. Wind field and Ekman depth were averaged over the study region (80.5–82.5°N, 15–35°E).

promote a greater deepening of the mixed layer from mid-September to early December than in 2019. However, the model results also demonstrate the importance of air temperature and radiative fluxes, and initial conditions, i.e., the late summer hydrography. In 2015, wind speeds are relatively high in late September and early October, but mixed layer depth increases rapidly also during the calmer period in late October and early November. In 2017 by contrast, wind speeds are high throughout November, but mixed layer depth remains rather stable. 2012 and 2013 show little and high changes in mixed layer depth, respectively, when initiated from the CTD profile measured in those years, but considerably larger versus smaller changes, respectively, when starting from the same profile.

Peralta-Ferriz and Woodgate (2015) discuss extensively the connection (or lack thereof) between mixed layer depth and wind speed in the Arctic Ocean. They suggest that the relationship is weak; correlations are significant only for open water conditions, and the relationship is strongly affected by presence of sea ice (see also Rainville and Woodgate, 2009; Rainville et al., 2011). Transfer of momentum from atmosphere to ocean through sea ice is highly complex, however. While Martin et al. (2014) suggested that there might be an optimum sea ice concentration for maximum momentum transfer, they followed this up in Martin et al. (2016) and showed that sea ice properties such as surface and bottom roughness and internal strength and form drag alter the momentum transfer. If we add the impact of snow, e.g., by smoothing the sea ice surface and altering light transfer, implications for primary production become even more complicated.

4.2. Sea ice conditions and surface chl a concentrations in the study region and upstream

While we do not have detailed information or time series data of sea ice characteristics such as thickness and roughness along our transects, we can investigate the general development of sea ice coverage in our study region using satellite-derived ice concentration data. Satellite-based observations allow us to put our measurements in a larger spatial and temporal context, linking our late summer and early winter measurements to seasonal sea ice and spring bloom dynamics. Sea ice modulates heat, momentum and gas exchange between ocean and atmosphere (Meyer et al., 2017; Renner et al., 2018; Martin et al., 2014; Fransson et al., 2009), limits light availability for primary producers in the upper ocean (Nicolaus et al., 2012; Castellani et al., 2022), and provides biological material (ice algae, organic matter, sediments) to seed blooms at the ice edge and in the marginal ice zone (Leu et al., 2015; Lannuzel et al., 2020). To take into account the impact of the AW inflow regarding advection of nutrients and phytoplankton (also consuming nutrients upstream along the AW inflow) (Renner et al., 2018; Vernet et al., 2019), we include the region to the west of our transect in our analyses of sea ice conditions and chl_{sat} distribution throughout the year leading up to the ship campaigns.

As sea ice impacts primary productivity directly by limiting light in the upper ocean, we take a closer look into the development of sea ice concentration in the region prior to the time of sampling in late summer. Light can efficiently enter the upper ocean through leads in drift ice (Castellani et al., 2022), we therefore choose a threshold of 50% ice concentration to assess whether or not a location can be considered "ice-free" with respect to availability of "sufficient" light. While this threshold is chosen rather arbitrarily, it aims to take into account the effects of, e.g., opening up of the ice pack, snow melt, and development of melt ponds during spring and summer on the pelagic light regime and thus primary production (Nicolaus et al., 2012; Assmy et al., 2017). Our analyses are not sensitive to the exact number, but a value of 50% ensured that we captured approximately the onset of ice retreat instead of a short-term decrease as could be the case with

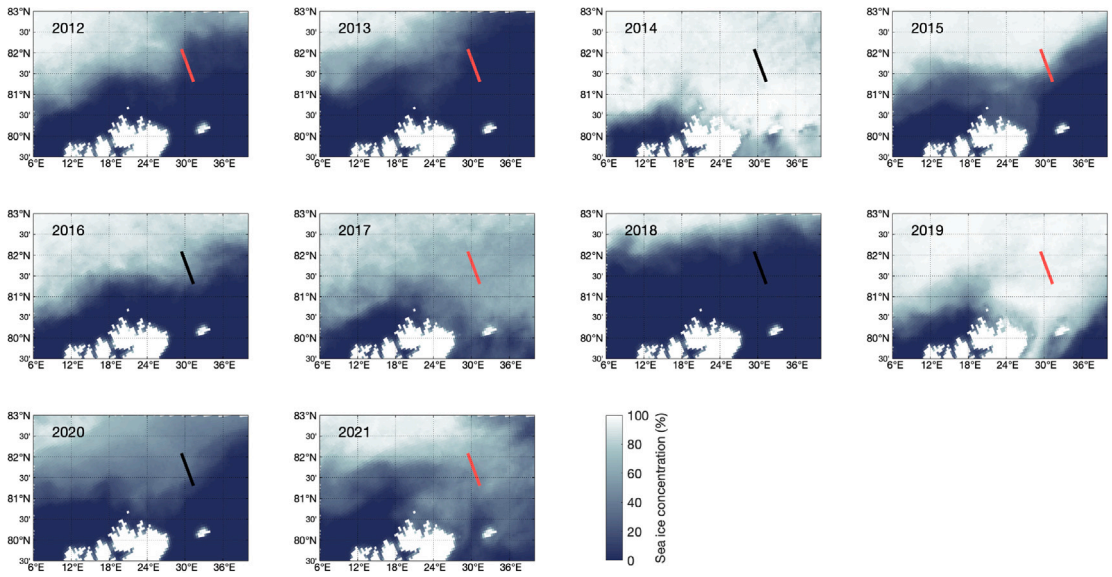

Fig. 9. Average sea ice concentration in the 60 days prior to 15 September for each year 2012–2021. The solid line indicates the position of the repeat transect (red for years with CTD and nutrient sampling, black for years without ship-based observations).

a higher threshold. Fig. 9 shows average sea ice concentrations for the 60-day period prior to 15 September, approximately the date of nutrient sampling for the late summer campaigns. Sea ice concentration was highly variable throughout the 2012–2021 period. In most years, ice concentrations on the shelf were <50% for about two months prior to 15 September (Supplementary Figure S5), whereas the deep part of the transect was ice-free for less than a month. The years 2014 and 2019 stand out with near complete ice coverage throughout the entire year. Only a small region over the shelf in the southwestern corner of our box had sea ice concentration below 50% in the week prior to 15 September. In 2018, and to a lesser degree in 2016, the opposite occurred with very little to no ice over the entire shelf and slope and into the deep basin over the entire year.

The chl_{sat} observations give an indication of the seasonal change of phytoplankton concentrations and bloom development even though they likely underestimate phytoplankton biomass due to presence of sea ice, lack of detection of under-ice blooms and vertical extent of phytoplankton distribution such as subsurface chl *a* maximum (Kahru et al., 2016; Ardyna et al., 2020; Bouman et al., 2020). Fig. 10 shows time series of satellite-derived average sea ice and chl_{sat} concentrations in a box north of Svalbard (Fig. 1) as well as measured chl *a* from the bottle samples. Spikes in chl_{sat} occur in general after a drop of sea ice concentrations, likely linked to the sudden change in ice regime and potential seeding of the pelagic bloom by ice algae (Leu et al., 2011). However, there is large variability regarding the magnitude of both the sea ice reduction and the subsequent chl_{sat} spike. Years with an extensive and persistent ice cover (2014, 2017, 2019, 2020) are often characterised by low chl_{sat} concentrations, especially when sea ice retreated late or only partially, as in 2014 and 2019 (Figure S5). Even when the pack ice is slightly less dense (2015, 2021), chl_{sat} concentrations remain relatively low. By contrast, the slightly earlier retreat in 2017 is followed by a delayed rise in chl_{sat}, opposing previous observations where earlier ice melt would result in an earlier, meltwater-induced spring bloom (e.g., Chierici et al., 2019). We could speculate that the relatively slow ice retreat in 2017 failed to produce a distinct meltwater layer at first (potentially mixed or advected away), and a longer period of meltwater accumulation was necessary to provide sufficient stratification. However, this delay could also be an artefact of the satellite measurements: due to the extensive ice cover, satellite data points are limited (Figure S1) and an earlier bloom development, potentially under sea ice or in leads, might have been missed. In 2020, the drop in ice concentrations occurred at a similar time as in 2017 but no bloom is observed. This could be connected to the extensive sea ice cover throughout the winter before which might have limited autumn and winter mixing, also indicated by lower nutrient concentrations in the surface layer and stronger stratification observed in November 2019 compared to the other early winter cruise in November 2021 (Figs. 4, 5). By contrast, years with very low ice coverage (2016, 2018) experience high chl_{sat} levels already from early spring and, in the case of 2018 when the ice edge was located far north (Fig. 9), throughout summer.

Satellite data only capture the surface, whereas our bottle data reveal chl *a* below the surface and provide information on the phase of the bloom and degradation state of the phytoplankton material (Figs. 7, S4). Especially in 2012 and 2017, the chl *a* maximum was at or just below the pycnocline and strongest over the deeper part of the transect while 2013 has a pronounced maximum in the near-surface over the slope. Phaeophytin proportions were high in all years, with the highest values observed in AW-derived water masses and lowest in surface waters. Gaffey et al. (2022) investigated bloom dynamics in the Pacific Arctic using satellite- and water sample-derived chl *a* and set a phaeophytin proportion threshold of 28% to characterise a mature bloom. Our samples indicate significantly higher proportions (>44% in the upper 10 m and 45% in the combined PSW and wPSW), suggesting a senescent bloom in agreement with the chl_{sat} time series. Surface nutrient concentrations, vertical distribution of chl *a* and size-fractionated chl *a* point to bloom to post-bloom conditions in early September according to the categorisation by Dybwad et al. (2021). Gaffey et al. (2022) further found that years with more sea ice (years with high sea ice concentrations and late breakup) were associated with larger phaeophytin proportion in mid-summer (July) than low sea ice years. However, they also point out large interannual variability and the importance of other factors such as stratification and nutrient availability. While our ship-borne dataset of chl *a* and phaophytin is limited to four years of observations collected in late summer (though similar timing relative to sea ice breakup) and one year in early winter, we see similar patterns: 2012 and 2013 are years with relatively low sea ice concentrations, early breakup and low phaeophytin proportions compared to 2015 and 2017. Interestingly, 2015 stands out with the highest proportion of phaeophytin both at the surface and throughout the water column (except in PSW), following very high ice concentrations during the autumn and early winter 2014–2015, and matching the high proportions observed on the Pacific side with very different sea ice dynamics (Gaffey et al., 2022).

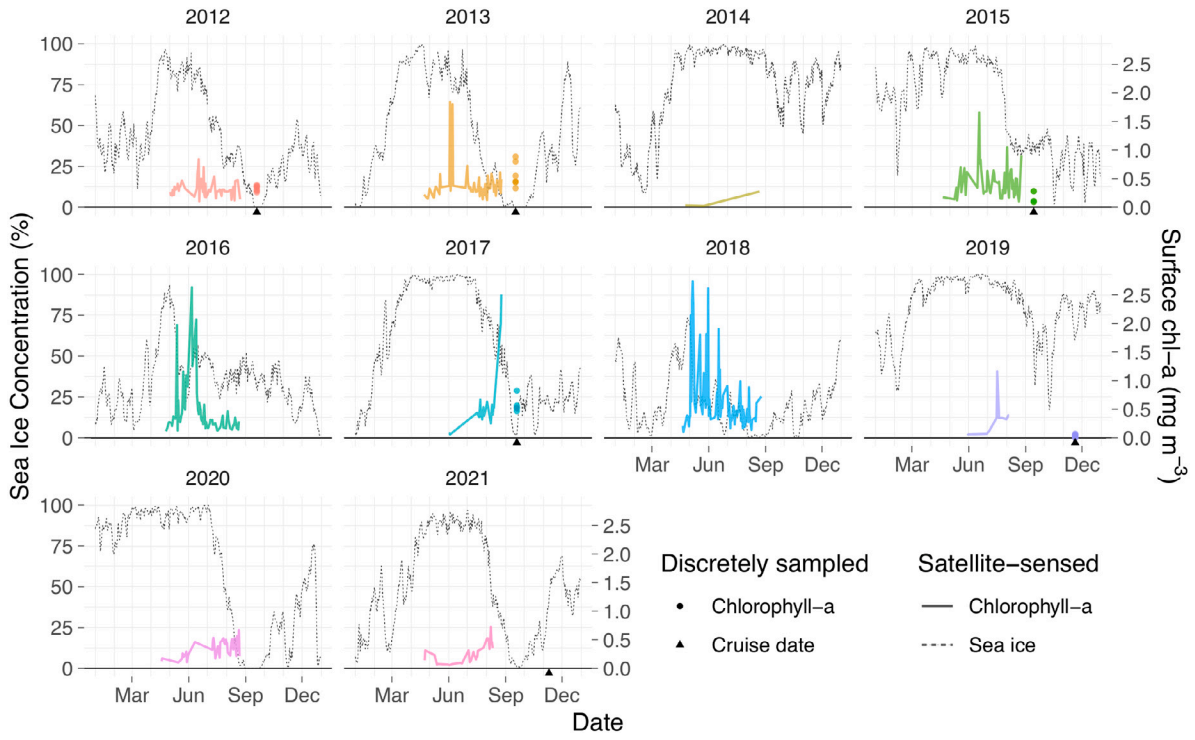

Fig. 10. Average daily, satellite-derived surface chl *a* concentrations (chl_{sat}; mg m^{-3}) in the quadrant 80.5–82.5°N by 15–35°E from April–August colour-coded by year (no observations are available during September–March due to low sun elevation angle/lack of sunlight), and daily sea ice concentration (dashed grey lines) for the same area. The dates of the cruises are indicated by black triangles. Bottle sample values (dots) are included for reference.

Henley et al. (2020) and Dybwad et al. (2022) found drawdown of nitrate and bloom initiation to occur at the same time at two long-term moorings deployed in the AW inflow north of Svalbard where one was deployed further west in year-round open water and the other further east experiencing seasonal sea ice cover. They suggested that deeper mixing in ice-free open-water conditions leads to reduced light for algal growth as algae are mixed down to greater depth, and delays the onset of the bloom to the time when sea ice melt facilitates stratification and a shallower mixed layer, enabling phytoplankton growth at the eastern mooring. Our data reflect the connection between sea ice extent, concentrations and timing of retreat and onset of the spring bloom. Late onset in open water in 2018 (as also observed by Henley et al., 2020; Dybwad et al., 2022) was probably due to lack of stratification, while late onset in 2017 with earlier ice melt may be due to under-ice blooms. However, to detect and confirm the role of under-ice blooms and timing of nutrient drawdown, time series observations under the sea ice are required, e.g., by moored nitrate sensors.

4.3. Impact of sea ice variability on surface layer properties and stratification

A more indirect impact of sea ice on primary productivity and thus phytoplankton concentrations is the effect on hydrography and stratification. A close ice pack hinders wind-driven mixing whereas thinner and more mobile drift ice can increase drag and thus momentum transfer (Martin et al., 2014). Mixing can then lead to weakening of stratification, deepening of the surface mixed layer, and transport of nutrients to the surface (Randelhoff et al., 2020). Light limitation by dense pack ice also inhibits heat transfer into the surface ocean and thermal stratification. On the other hand, sea ice formation and melt will affect the surface layer by increasing and decreasing salinity, respectively. A fresh melt layer can efficiently cap off the layer below from the surface, thus limiting nutrient flux to the surface layer and restricting primary production to the potentially deeper part of the euphotic layer below. At the same time, the transect lies in a highly advective region and thus also reflects processes taking place upstream, both regarding advected water masses and sea ice drift (Randelhoff et al., 2018; Renner et al., 2018; Lundesgaard et al., 2021), and ice-ocean processes that influence carbon and nutrient cycling along the AW inflow (Jones et al., 2021, 2023).

The autumn and winter seasons 2014–2015 and 2019–2020 were characterised by extensive sea ice cover also throughout the low-ice season (August–January). Lundesgaard et al. (2021) note that the high sea ice concentration anomalies were connected to large import of sea ice from the central Arctic, due to an eastward deflection of the Transpolar Drift towards our study region. When this sea ice meets the AW north of Svalbard, the upward heat flux leads to melt and input of cold and fresh surface water, thus increasing stratification and reducing vertical exchange (Renner et al., 2018; Lind et al., 2018) and potentially explaining the strong stratification in November 2019 compared to November 2021.

To look closer into the persistence of the sea ice cover from winter until late summer to investigate the potential impact of enhanced or reduced momentum transfer on stratification and thus potential vertical flux, we define the date of summer retreat by the last day of ice concentrations above 80% before 15 September of the years with hydrographic observations. Then, 2012 and 2013 appear similar with retreat around the month shift June–July; 2015, 2017 and 2021 experience slightly later retreat in late July or early August; and 2019 stands out with ice concentrations above 80% until early September. However, in 2012, average ice concentrations were less often above 90% than in 2013, both temporally and spatially, and the duration of ice coverage with concentration >80% was only just over 50 days compared to 80 days in 2013. Along with the different properties of the AW inflow (narrower and warmer core but colder from the deeper part of the slope northward) and colder and thicker PSW in 2013, this might have contributed to enhanced warming of the surface layer, greater momentum transfer from atmosphere to ocean through wind-driven mixing, and a deeper mixed layer in 2012. In 2015 and 2017, sea ice concentrations were above 80% for 139 and 140 days, respectively,

but the ice pack was denser in 2017 with 118 days of concentrations >90% (in 2015: 84 days). While the mixed layer depth appears similar in both years over the deeper part of the transect, the cold and fresh surface layer is far more pronounced and extending onto the shelf in 2017. This supports the sea ice budget analyses by Lundesgaard et al. (2021) who show that in 2017, a large amount of sea ice was lost in the area, and our result indicates that much of this ice was melted, leading to strong stratification over the entire transect.

4.4. Connecting physics and biology and role of regional versus large-scale processes

The four years with late summer observations of hydrography, nutrient and chl *a* concentrations are characterised by similar levels of chl_{sat} concentrations integrated over the summer (calculated as the time integral of the chl_{sat} time series shown in Fig. 10 per year) and similar timing of sea ice retreat and thus ice-free period prior to sampling. However, the years differ considerably regarding winter-to-summer sea ice coverage, stratification, bloom development and in situ chl *a* and phaeophytin levels, and nutrient concentrations (especially below the nitracline) and ratios.

While we do not have observations of the phytoplankton community along our transects, nutrient ratios might give an indication of dominant species as well as resupply processes. Redfield et al. (1963) suggested idealised ratios for carbon to nitrate to phosphate (C:N:P) of 106:16:1 in marine organisms, and Brzezinski (1985) modified these for diatoms to include silicate (C:Si:N:P = 106:15:16:1). The idealised ratios are included in Fig. 6. Averaged across the entire transects, our late summer N/P ratios in all years were below Redfield values, whereas winter ratios were close to or slightly above the Redfield ratio of N/P = 16. Si/N ratios were below the Redfield–Brzezinski ratio (Si/N = 0.94) in all years, summer and winter. The low summer nutrient ratios especially in 2012, 2015 and 2017 are indicative of diatom production under nutrient-replete conditions (Brzezinski, 1985). The spring blooms in our region are typically dominated by diatoms or *Phaeocystis pouchetii*, which is an important non-silicate phytoplankton species in the region (Degerlund and Eilertsen, 2010; Assmy et al., 2017). Silicate could be the limiting nutrient for diatoms during blooms, if they dominate the phytoplankton assemblage and consume Si/N in ratios >1; our ratios in all late summer situations were <1. Diatoms dominate over *Phaeocystis pouchetii* when sufficient silicate is present ([$SiOH_4$ > 2 μM]) (Egge and Aksnes, 1992). Nevertheless, Reigstad et al. (2002) showed that diatom blooms sometimes do not deplete silicate, and that physical effects explained the variability in concentrations and ratios. Interannual variability and local differences in mixing may favour *Phaeocystis pouchetii* over diatoms and can affect the nutrient uptake ratios with nitrate depletion in presence of available silicate (Reigstad et al., 2002). In our data, we see a generally nitrate-limited system where N/P and Si/N ratios suggest a mostly diatom dominated phytoplankton community. 2013 with higher N/P and lower Si/N might have experienced a larger influence of *Phaeocystis pouchetii* (Tremblay et al., 2015).

The early winter transects in 2019 and 2021 showed a shift in nutrient ratios. The higher Si/N ratios might have resulted from lower silicate uptake during the growing season, and/or be a signal of dissolution of biogenic silica releasing silicate from diatom frustules (or mixing with high silicate water where dissolution has taken place) relative to rates of organic matter remineralisation releasing nitrate in subsurface waters (Jones et al., 2023). However, consistently lower Si/N relative to idealised ratios in both late summer and early winter across our transects indicate the impact of diatoms (Tremblay et al., 2015) and uptake of silicate during the growing season and resupply of nitrate before resupply of silicate due to faster remineralisation than silica dissolution.

The considerable spatial variability in nutrient distribution and ratios across the transects also reflects different physical drivers from the shelf into the deep basin, which act differently from year to year. 2012 and 2013 experienced a less extensive sea ice cover than 2015 and 2017, and late summer hydrography shows a deeper mixed layer and deeper nitracline in those low ice years as well. However, the pattern along the transect differs considerably with shallower mixed layer and a shallower upper AW boundary in 2013 further north (Figs. 2, 4). At the same time, 2013 is characterised by higher nitrate and lower phosphate and silicate concentrations in the relatively cold and fresh AW and in the surface waters compared to 2012 (Tables S1 and S2), and N/P and Si/N ratios show large variability by latitude (Fig. 6). We suggest that a combination of an anomaly in the inflowing AW properties and large-scale circulation patterns connected to displacement of the Transpolar Drift (Wilson et al., 2021) might have led to unusual water mass distribution especially along the northern, deep part of our transect, potentially impacting particularly the water masses from the surface to and including the (upper part of the) AW layer and causing the high fraction of modified Atlantic water in 2013 (Fig. 3). While a direct impact of riverine input of nutrients is unlikely in our study region, processes on the Siberian shelf such as primary production, denitrification, mixing, remineralisation and benthic cycling can modify nutrient concentrations in surface waters and sea ice formed there (Tremblay et al., 2015; Tuerena et al., 2022). Advection of sea ice and surface waters with the Transpolar Drift spreads this signature of relatively low nitrate and high silicate and phosphate concentrations across the Central Arctic Ocean towards Fram Strait (Charette et al., 2020). The slightly elevated silicate and Si/N in the PSW/wPSW surface layer in 2021 relative to the other years could have resulted from contributions from the Transpolar Drift (Charette et al., 2020), which was deflected prior to the study period. A similar enhanced silicate signal was found in the Barents Sea in summer 2021 (Koenig et al., 2023). Additionally, the signal could have resulted from blooms of the haptophyte *Phaeocystis pouchetii*. We suggest that the variability in the location of the Transpolar Drift (Wilson et al., 2021), which is strongly influenced by the large-scale atmospheric circulation in the Arctic Ocean (Wang and Danilov, 2022) can potentially lead to episodic input of Siberian-influenced surface waters at least to the deeper parts of our study region.

The relatively high ice years 2015 and 2017 experienced a slightly later sea ice retreat than 2012 and 2013 and accordingly later bloom start and peak (Figs. 10, S5). The stratification was strong with a shallow mixed layer depth in both 2015 and 2017, except for above the slope in 2015 (Fig. 4). The surface layer differed considerably between both years though with a cold and fresh layer over the entire transect in 2017 (Fig. 2). Interestingly, both years showed slightly higher nutrient concentrations in the surface waters than 2012 and 2013 (PSW and wPSW; Fig. 11, Table S2) but significant lower concentrations in the AW layer in 2015 compared to 2017; while the higher surface nutrient concentrations in 2017 corresponded with lower chl_{sat} integrated over the summer (potentially indicating less consumption) compared to 2015, the high nutrient concentrations in the AW layer in 2017 might have contributed the slightly elevated values in the PSW. Other markers such as high phaeophytin proportion and low fraction of >10 μm chl *a* implying larger proportion of small phytoplankton in 2015 compared to 2017 suggest a later bloom stage and/or larger impact of grazing leading to degradation. Further upstream northwest of Svalbard, Jones et al. (2021) show high levels of primary production in August 2015, leading to low nitrate levels in the AW. In 2017 by contrast, their surface chl *a* concentrations were lower, and they suggest a greater role of meteoric water input and mixing. Our transects were covered approximately two to three weeks later in the respective years, and we suggest that the large advective component of the AW inflow for hydrography (e.g., Renner et al., 2018), nutrients (Henley et al., 2020), phytoplankton (Vernet et al., 2019) and grazers (Wassmann et al., 2015; Dybwad et al., 2022) strongly impacted our observations.

The early winter sampling years 2019 and 2021 were also two of the three years with lowest chl_{sat} integrated over the summer (only 2014

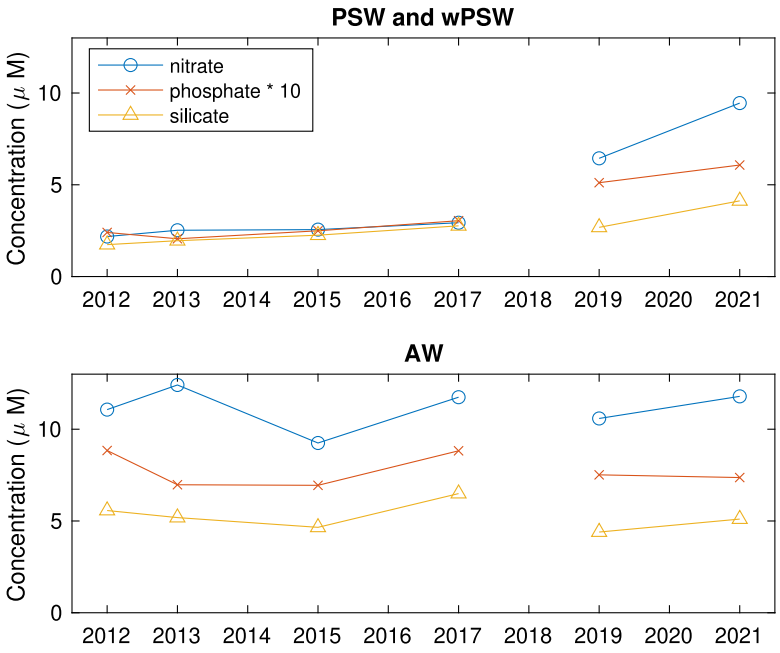

Fig. 11. Average nutrient concentrations in PSW and wPSW (upper panel) and AW (lower panel).

is lower), due to extensive and persistent sea ice coverage throughout 2019 and relatively late retreat in 2021. The difference in sea ice coverage and hydrography with stronger stratification in 2019 compared to 2021 (though reduced compared to the summer transects) was consistent with nutrient concentrations in the surface layers: While concentrations in the AW layer were similar to the other years, concentrations in PSW/wPSW were higher (Fig. 11, Table S2). Contraction of the upper layers in the *T–SA* diagrams (Fig. 3) and lower N^2 than in summer (Fig. 4) were present in both years but stronger in 2021, supporting more advanced upward mixing (possibly due to stronger winds as discussed above) and beginning re-supply to the surface from below in 2021 than in 2019 even though sampling took place 10 days later in 2021. The difference in phytoplankton biomass and nutrient consumption over summer between the two years was likely overridden by physical processes driving vertical nutrient flux (Randelhoff et al., 2020).

4.5. Potential for autumn blooms with changing sea ice

The general increase in primary production across the Arctic Ocean (e.g., Lewis et al., 2020) is accompanied and at least partially driven by a longer growth season due to longer ice-free periods (Arrigo and van Dijken, 2015) and by changes in phytoplankton phenology, including earlier onset of spring blooms due to earlier melt (Lannuzel et al., 2020) and increased occurrence of autumn blooms (Ardyna et al., 2014). These changes at the very base of the food web have implications for the functioning of the Arctic ecosystem and are therefore critical for assessment of future trends (Wassmann and Reigstad, 2011).

Gaffey et al. (2022) showed for the northern Bering Sea that overall, earlier sea ice breakup and low winter ice concentrations lead to later onset of open water spring bloom and increase in early bloom stages in mid-summer, whereas late ice retreat drives early ice-associated blooms. For individual years though, nutrient availability and stratification are the dominant drivers for bloom development. Our data from the other side of the Arctic suggest similar patterns with regards to timing of sea ice retreat and bloom occurrence. However, given the higher latitude of our observations and thus later sea ice retreat and light availability we reach similar stages in bloom development considerably later in the year, limiting the length of the growing season.

Waga and Hirawake (2020) observed increased occurrence of autumn blooms in the Chukchi Sea in 2003–2017, dependent on vertical re-supply from nutrient-rich near bottom waters. Tied to bathymetry, remineralisation of sinking material and autumn convection play a major role to bring nutrients back to the euphotic zone. On the Atlantic side, the shelf north of Svalbard and in the northern Barents Sea is deeper and thus less suitable for, e.g., shelf-break upwelling (Randelhoff and Sundfjord, 2018), and contributions from benthic processes like remineralisation are seasonally limited; Freitas et al. (2020) show strong pelagic–benthic coupling in the northern Barents Sea with high reactivity and regeneration of nutrients and organic material that contributes to replenishment of surface layers during winter deep convective mixing. Instead, the AW inflow provides a year-round source of nutrients. Orkney et al. (2022) highlight the importance of this source for autumn chl *a* concentrations and blooms in the Barents Sea while Randelhoff et al. (2018) state that advection of nutrients with AW alleviates light nutrient limitation north of Svalbard and increases primary production.

The reliance on the AW inflow as nutrient source for the Eurasian Arctic and even the Central Arctic Ocean raises concerns regarding trends in nutrient concentrations in the AW layer. Our time series is too short to assess trends, but demonstrates large variability in concentrations by water mass, similar to findings by Duarte et al. (2021). Our results suggest though that while AW clearly is a major source of nutrients for surface water, the mere presence of an AW layer is not sufficient when stratification is strong and limits vertical flux. Upwelling of nutrients can be driven by storm events (in the absence of sea ice), which are more frequent in autumn and can promote autumn mixing. Where this occurs early enough before light becomes limiting, autumn blooms can form (Castro de la Guardia et al., 2019). Also, enhanced autumn and winter mixing can promote higher nutrient concentrations in spring and thus larger blooms. While the enhancement (or suppression) of spring blooms might be seen in our combined time series of sea ice concentration and chl_{sat}, using low sea ice concentrations as a proxy for potential wind-driven mixing, we do not see signs of autumn blooms even when sea ice concentrations drop early in the productive season and allow early wind-driven mixing. Early September conditions at our latitudes (approx. 81.2-82°N) rather

resemble mature to post-bloom stages with nutrient-limitation in the surface layers, and we reckon that re-supply starts too late when light conditions become limiting as the sun set below the horizon in mid-October.

5. Conclusions

We presented data on hydrography, inorganic nutrient distributions and chl *a* concentrations from repeat measurements of a transect north of Svalbard crossing the AW inflow into the Arctic Ocean, covering the period 2012–2021. Late summer measurements show post-bloom conditions for both nutrients and chl *a*, while early winter observations show the beginning of breakdown of stratification and re-supply of nutrients towards the surface layer. However, there is large interannual variability both in hydrography and upper ocean nutrient and chl *a* concentrations. While the AW inflow and its properties play an important role in steering this variability below the surface and regional winds impact the mixed layer, the sea ice cover in the region and its development over summer dominates signals at the surface by impacting bloom dynamics, stratification and import of surface waters from the Central Arctic Ocean. The advective regime of the AW inflow and advection of sea ice are major factors in the marine system north of Svalbard which can overrule local physical, chemical, and biological processes. With ongoing Atlantification, we can expect characteristics of the region north of Svalbard to spread eastward in the Eurasian Basin, including reduced sea ice cover and stronger influence of AW with its transport of nutrients and organisms. However, primary production along the AW pathway has the potential to deplete nutrients in the euphotic part of the AW layer while the layer extends to the surface and thus reduce nutrient concentrations advected downstream. Re-supply of nutrients may occur as soon as wind-driven mixing and winter convective mixing break down summer stratification. However, the timing and extent of wind-driven mixing and its efficiency in deepening the mixed layer are highly variable and impacted by the sea ice cover. We suggest that unlike on the Pacific inflow shelves of the Arctic Ocean (e.g., Waga and Hirawake, 2020), the weakening of stratification is still unlikely to occur early enough to allow the development of autumn blooms due to limited light availability at the high latitude of the AW inflow region.

Declaration of competing interest

The authors declare that they have no known competing financial interests or personal relationships that could have appeared to influence the work reported in this paper.

Data availability

CTD data are available at Pavlov et al. (2017a,b) (hydrography for 2012 and 2013, respectively), Renner and Pavlov (2023a,b) (chl *a* fluorescence for 2012 and 2013, respectively) Sundfjord (2022, 2023c) (CTD hydrography and chl *a* fluorscence for 2019 and 2021). Water sample data for inorganic nutrients and chlorophyll *a* for 2012, 2013, 2019 and 2021 are available at Reigstad et al. (2023a,b,c) and Chierici et al. (2023), respectively. Combined datasets for CTD hydrography, water sample inorganic nutrients and chlorophyll *a* for 2015 and 2017 are available at Sundfjord et al. (2023a,b), respectively.

Acknowledgements

This study was funded through the Fram Centre Arctic Ocean flagship project A-TWAIN (project no. 66050) and the Research Council of Norway project Nansen Legacy (RCN 276730). We thank the captains, crews and science teams of RV Lance and RV Kronprins Haakon. Particular thanks to Sigrid Øygarden for the BGC sampling and to Kristine Cerbule and Claire Mourgues for stepping in when Sigrid could not join. Thanks go also to Ingrid Wiedmann, Karen Assmann, Øyvind Lundesgaard and Morven Muilwijk for useful discussions at various stages in the manuscript writing, and to two anonymous reviewers and the editor for thoughtful and constructive reviews. We thank the NASA Ocean Biology group for making their ocean colour data publicly and freely available.

Appendix A. Supplementary data

Supplementary material related to this article can be found online at https://doi.org/10.1016/j.pocean.2023.103162.

References

Ardyna, M., Arrigo, K.R., 2020. Phytoplankton dynamics in a changing Arctic Ocean. Nature Clim. Change 10, 892–903. http://dx.doi.org/10.1038/s41558-020-0905-y.

Ardyna, M., Babin, M., Gosselin, M., Devred, E., Rainville, L., Tremblay, J.-É., 2014. Recent Arctic Ocean sea ice loss triggers novel fall phytoplankton blooms. Geophys. Res. Lett. 41, 6207–6212. http://dx.doi.org/10.1002/2014GL061047.

Ardyna, M., Mundy, C.J., Mayot, N., Matthes, L.C., Oziel, L., Horvat, C., Leu, E., Assmy, P., Hill, P.A., Gale, M., Melnikov, I.A., Arrigo, K.R., 2020. Under-ice phytoplankton blooms: Shedding light on the "invisible" part of Arctic primary production. Front. Mar. Sci. 7, 608032. http://dx.doi.org/10.3389/fmars.2020.608032.

Arrigo, K.R., van Dijken, G.L., 2015. Continued increases in Arctic Ocean primary production. Prog. Oceanogr. 136, 60–70. http://dx.doi.org/10.1016/j.pocean.2015.05.002.

Assmy, P., Fernández-Méndez, M., Duarte, P., Meyer, A., Randelhoff, A., Mundy, C.J., Olsen, L.M., Kauko, H.M., Bailey, A., Chierici, M., Cohen, L., Doulgeris, A.P., Ehn, J.K., Fransson, A., Gerland, S., Hop, H., Hudson, S.R., Hughes, N., Itkin, P., Johnsen, G., King, J.A., Koch, B.P., Koenig, Z., Kwasniewski, S., Laney, S.R., Nicolaus, M., Pavlov, A.K., Polashenski, C.M., Provost, C., Rösel, A., Sandbu, M., Spreen, G., Smedsrud, L.H., Sundfjord, A., Taskjelle, T., Tatarek, A., Wiktor, J., Wagner, P.M., Wold, A., Steen, H., Granskog, M.A., 2017. Leads in Arctic pack ice enable early phytoplankton blooms below snow-covered sea ice. Sci. Rep. 7, 40850. http://dx.doi.org/10.1038/srep40850.

Beszczynska-Möller, A., Fahrbach, E., Schauer, U., Hansen, E., 2012. Variability in Atlantic water temperature and transport at the entrance to the Arctic Ocean, 1997–2010. ICES J. Mar. Sci. 69 (5), 852–863. http://dx.doi.org/10.1093/icesjms/fss056.

Biddle, L.C., Heywood, K.J., Kaiser, J., 2017. Glacial meltwater identification in the Amundsen Sea. J. Phys. Oceanogr. 47, 933–954. http://dx.doi.org/10.1175/JPO-D-16-0221.1.

Bouman, H.A., Jackson, T., Sathyendranath, S., Platt, T., 2020. Vertical structure in chlorophyll profiles: influence on primary production in the Arctic Ocean. Philos. Trans. A 378, 20190351. http://dx.doi.org/10.1098/rsta.2019.0351.

Brzezinski, M.A., 1985. The Si:C:N ratios of marine diatoms: interspecific variability and the effect of some environmental variables. J. Phycol. 21, 345–357. http://dx.doi.org/10.1111/j.0022-3646.1985.00347.x.

Castellani, G., Veyssière, G., Karcher, M., Stroeve, J., Banas, S.N., Bouman, A.H., Brierley, S.A., Connan, S., Cottier, F., Große, F., Hobbs, L., Katlein, C., Light, B., McKee, D., Orkney, A., Proud, R., Schourup-Kristensen, V., 2022. Shine a light: Under-ice light and its ecological implications in a changing Arctic Ocean. Ambio 51, 307–317. http://dx.doi.org/10.1007/s13280-021-01662-3.

Castro de la Guardia, L., Garcia-Quintana, Y., Claret, M., Hu, X., Galbraith, E.D., Myers, P.G., 2019. Assessing the role of high-frequency winds and sea ice loss on Arctic phytoplankton blooms in an ice-ocean-biogeochemical model. J. Geophys. Res.: Biogeosci. 124, 2728–2750. http://dx.doi.org/10.1029/2018JG004869.

Charette, M.A., et al., 2020. The Transpolar Drift as a source of riverine and shelf-derived trace elements to the Central Arctic Ocean. J. Geophys. Res.: Oceans 125 (5), http://dx.doi.org/10.1029/2019JC015920, e2019JC015920.

Chierici, M., Renner, A.H.H., Mourgues, C., 2023. Dissolved inorganic nutrients (nitrate, phosphate and silicic acid) from the combined Nansen Legacy and A-TWAIN Mooring service cruise November 2021 [data set]. Norwegian Polar Institute, http://dx.doi.org/10.21334/npolar.2023.caee8992.

Chierici, M., Vernet, M., Fransson, A., Børsheim, K.Y., 2019. Net community production and carbon exchange from winter to summer in the Atlantic Water inflow to the Arctic Ocean. Front. Mar. Sci. 6, 528. http://dx.doi.org/10.3389/fmars.2019.00528.

Cole, S.T., Toole, J.M., Lele, R., Timmermans, M.-L., Gallaher, S.G., Stanton, T.P., Shaw, W.J., Hwang, B., Maksym, T., Wilkinson, J.P., Ortiz, M., Graber, H., Rainville, L., Petty, A.A., Farrell, S.L., Richter-Menge, J.A., Haas, C., 2017. Ice and ocean velocity in the Arctic marginal ice zone: Ice roughness and momentum transfer. Elementa Sci. Anth. 5, 55. http://dx.doi.org/10.1525/elementa.241.

Degerlund, M., Eilertsen, H.C., 2010. Main species characteristics of phytoplankton spring blooms in NE Atlantic and Arctic waters (68-80 N). Eastuaries Coasts 33, 242–269. http://dx.doi.org/10.1007/s12237-009-9167-7.

Duarte, P., Meyer, A., Moreau, S., 2021. Nutrients in water masses in the Atlantic sector of the Arctic Ocean: Temporal trends, mixing and links with primary production. J. Geophys. Res.: Oceans 126, http://dx.doi.org/10.1029/2021JC017413, e2021JC017413.

Dybwad, C., Assmy, P., Olsen, L.M., Peeken, I., Nikolopoulos, A., Krumpen, T., Randelhoff, A., Tatarek, A., Wiktor, J., Reigstad, M., 2021. Carbon export in the seasonal sea ice zone north of Svalbard from winter to late summer. Front. Mar. Sci. 7, 525800. http://dx.doi.org/10.2289/fmars.2020.525800.

Dybwad, C., Lalande, C., Bodur, Y.V., Henley, S.F., Cottier, F., Ershova, E.A., Hobbs, L., Last, K.S., Dabrowska, A.M., Reigstad, M., 2022. The influence of sea ice cover and Atlantic Water advection on annual particle export north of Svalbard. J. Geophys. Res.: Oceans 127, http://dx.doi.org/10.1029/2022JC018897, e2022JC018897.

Egge, J.K., Aksnes, D.L., 1992. Silicate as regulating nutrient in phytoplankton competition. Mar. Ecol. Prog. Ser. 83, 281–289.

Fransson, A., Chierici, M., Nojiri, Y., 2009. New insights into the spatial variability of the surface water carbon dioxide in varying sea ice conditions in the Arctic Ocean. Cont. Shelf Res. 29 (10), 1317–1328. http://dx.doi.org/10.1016/j.csr.2009.03.008.

Freitas, F.S., Hendry, K.R., Henley, S.F., Faust, J.C., Tessin, A.C., Stevenson, M.A., Abbott, G.D., März, C., Arndt, S., 2020. Benthic-pelagic coupling in the Barents Sea: An integrated data-model framework. Phil. Trans. R. Soc. A 378, 20190359. http://dx.doi.org/10.1098/rsta.2019.0359.

Gaffey, C.B., Frey, K.E., Cooper, L.W., Grebmeier, J.M., 2022. Phytoplankton bloom stages estimated from chlorophyll pigment proportions suggest delayed summer production in low sea ice years in the northern Bering Sea. PLoS ONE 17 (7), e0267586. http://dx.doi.org/10.1371/journal.pone.0267586.

Gundersen, K., Møgster, J.S., Lien, V.S., Ershova, E., Lunde, L.F., Arnesen, H., Olsen, A.-K., 2022. Thirty years of nutrient biogeochemistry in the Barents Sea and the adjoining Arctic Ocean, 1990–2019. Sci. Data 9:649. http://dx.doi.org/10.1038/s41597-022-01781-w.

Hátún, H., Azetsu-Scott, K., Somavilla, R., Rey, F., Johnson, C., Mathis, M., Mikolajewicz, U., Coupel, P., Tremblay, J.-É., Hartman, S., Pacariz, S.V., Salter, I., Ólafsson, J., 2017. The subpolar gyre regulates silicate concentrations in the North Atlantic. Sci. Rep. 7, 14576. http://dx.doi.org/10.1038/s41598-017-14837-4.

Henley, S.F., Porter, M., Hobbs, L., Braun, J., Cuillaume-Castel, R., Venables, E.J., Dumont, E., Cottier, F., 2020. Nitrate supply and uptake in the Atlantic Arctic sea ice zone: seasonal cycle, mechanisms and drivers. Phil. Trans. R. Soc. A 378, 20190361. http://dx.doi.org/10.1098/rsta.2019.0361.

Hersbach, H., Bell, B., Berrisford, P., Biavati, G., Horá nyi, A., Muñ oz Sabater, J., Nicolas, J., Peubey, C., Radu, R., Rozum, I., Schepers, D., Simmons, A., Soci, C., Dee, D., Thé paut, J.N., 2023a. ERA5 hourly data on pressure levels from 1940 to present. http://dx.doi.org/10.24381/cds.bd0915c6.

Hersbach, H., Bell, B., Berrisford, P., Biavati, G., Horá nyi, A., Muñ oz Sabater, J., Nicolas, J., Peubey, C., Radu, R., Rozum, I., Schepers, D., Simmons, A., Soci, C., Dee, D., Thé paut, J.N., 2023b. ERA5 hourly data on single levels from 1940 to present. http://dx.doi.org/10.24381/cds.adbb2d47.

Holm-Hansen, O., Riemann, B., 1978. Chlorophyll a determination: Improvements in methodology. Oikos 30 (3), 438–447. http://dx.doi.org/10.2307/3543338.

Ingvaldsen, R.B., Assmann, K.M., Primicerio, R., Fossheim, M., Polyakov, I.V., Dolgov, A.V., 2021. Physical manifestations and ecological implications of Arctic Atlantification. Nature Rev. Earth Environ. 2, 874–889. http://dx.doi.org/10.1038/s43017-021-00228-x.

IOC, SCOR, IAPSO, 2010. The International Thermodynamic Equation of Seawater - 2010: Calculation and Use of Thermodynamic Properties. Intergovernmental Oceanographic Commission, Manuals and Guides No 56, UNESCO, 196pp.

Jakobsson, M., Mayer, L.A., Coakley, B., Dowdeswell, J.A., Forbes, S., Fridman, B., Hodnesdal, H., Noormets, R., Pedersen, R., Rebesco, M., Schenke, H.W., Zarayskaya, Y., Accettella, D., Armstrong, A., Anderson, R.M., Bienhoff, P., Camerlenghi, A., Church, I., Edwards, M., Gardner, J.V., Hall, J.K., Hell, B., Hestvik, O.B., Kristoffersen, Y., Marcussen, C., Mohammad, R., Mosher, D., Nghiem, S.V., Pedrosa, M.T., Travaglini, P.G., Weatherall, P., 2012. The International Bathymetric Chart of the Arctic Ocean (IBCAO) version 3.0. Geophys. Res. Lett. 39, L12609. http://dx.doi.org/10.1029/2012GL052219.

Jones, E., Chierici, M., Fransson, A., Assmann, K., Renner, A., Lødemel, H., 2023. Inorganic carbon and nutrient dynamics in the marginal ice zone of the Barents Sea: seasonality and implications for ocean acidification. Prog. Oceanogr. 219, 103131. http://dx.doi.org/10.1016/j.pocean.2023.103131.

Jones, E.M., Chierici, M., Menze, S., Fransson, A., Ingvaldsen, R.B., Lødemel, H.H., 2021. Ocean acidification state variability of the Atlantic Arctic Ocean around northern Svalbard. Prog. Oceanogr. 199, 102708. http://dx.doi.org/10.1016/j.pocean.2021.102708.

Kahru, M., Lee, Z., Mitchell, B.G., Nevison, C.D., 2016. Effect of sea ice cover on satellite-detected primary production in the Arctic Ocean. Biol. Lett. 12, 20160223. http://dx.doi.org/10.1098/rsbl.2016.0223.

Koenig, Z., Muilwijk, M., Sandven, H., Lundesgaard, Ø., Assmy, P., Lind, S., Assmann, K.M., Chierici, M., Fransson, A., Gerland, S., Jones, E., Renner, A.H.H., Granskog, M.A., 2023. From winter to late summer in the northwestern Barents Sea shelf: Impacts of seasonal progression of sea ice and upper ocean on nutrient and phytoplankton dynamics. Prog. Oceanogr. 219, 103174. http://dx.doi.org/10.1016/j.pocean.2023.103174.

Lagnevall, S., 2017. The Effect of Surface Buoyancy Forcing on the Thermocline in the Amundsen Sea (M.Sc. thesis). Department of Marine Sciences, University of Gothenburg.

Lannuzel, D., Tedesco, van Leeuwe, L.M., Campbell, K., Flores, H., Delille, B., Miller, L., Stefels, J., Assmy, P., Bowman, J., Brown, K., Castellani, G., Chierici, M., Crabeck, O., Damm, E., Else, B., Fransson, A., Fripiat, F., Geilfus, N.X., Jacques, C., Jones, E., Kaartokallio, H., Kotovitch, M., Meiners, K., Moreau, S., Nomura, D., Peeken, I., Rintala, J.M., Steiner, N., Tison, J.L., Vancoppenolle, M., Van der Linden, F., Vichi, M., Wongpan, P., 2020. The future of Arctic sea-ice biogeochemistry and ice-associated ecosystems. Nature Clim. Change 10, 983–992. http://dx.doi.org/10.1038/s41558-020-00940-4.

Leu, E., Mundy, C.J., Assmy, P., Campbell, K., Gabrielsen, T.M., Gosselin, M., Juul-Pedersen, T., Gradinger, R., 2015. Arctic spring awakening - Steering principles behind the phenology of vernal ice algal blooms. Prog. Oceanogr. 139, 151–170. http://dx.doi.org/10.1016/j.pocean.2015.07.012.

Leu, E., Søreide, J., Hessen, D.O., Falk-Petersen, S., Berge, J., 2011. Consequences of changing sea-ice cover for primary and secondary producers in the European Arcric shelf seas: Timing, quantity, quality. Prog. Oceanogr. 90, 18–32. http://dx.doi.org/10.1016/j.pocean.2011.02.004.

Lewis, K.M., van Dijken, G.L., Arrigo, K.R., 2020. Changes in phytoplankton concentration now drive increased Arctic Ocean primary production. Science 369, 198–202. http://dx.doi.org/10.1126/science.aay8380.

Lind, S., Ingvaldsen, R.B., Furevik, T., 2018. Arctic warming hotspot in the northern Barents Sea linked to declining sea-ice import. Nature Clim. Change 8, 634–639. http://dx.doi.org/10.1038/s41558-018-0205-y.

Lundesgaard, Ø., Sundfjord, A., Renner, A.H.H., 2021. Drivers of interannual sea ice concentration variability in the Atlantic Water inflow region north of Svalbard. J. Geophys. Res. 126, http://dx.doi.org/10.1029/2020JC016522, e2020JC016522.

Martin, T., Steele, M., Zhang, J., 2014. Seasonality and long-term trend of Arctic Ocean surface stress in a model. J. Geophys. Res. 119, 1723–1738. http://dx.doi.org/10.1002/2013JC009425.

Martin, T., Tsamados, M., Schroeder, D., Feltham, D.L., 2016. The impact of variable sea ice roughness on changes in Arctic Ocean surface stress: A model study. J. Geophys. Res. Oceans 121, 1931–1952. http://dx.doi.org/10.1002/2015JC011186.

Meyer, A., Fer, I., Sundfjord, A., Peterson, A.K., 2017. Mixing rates and vertical heat fluxes north of Svalbard from Arctic winter to spring. J. Geophys. Res. 122, http://dx.doi.org/10.1002/2016JC012441.

Muilwijk, M., Nummelin, A., Heuzé, C., Polyakov, I.V., Zanowski, H., Smedsrud, L.H., 2023. Divergence in climate model projections of future Arctic atlantification. J. Clim. 36, 1727–1748. http://dx.doi.org/10.1175/JCLI-D-22-0349.s1.

NASA Goddard Space Flight Center, O.B.P.G., 2022. Moderate-resolution Imaging Spectroradiometer (MODIS) Aqua Chlorophyll Data. NASA OB.DAAC, Greenbelt, MD, USA, http://dx.doi.org/10.5067/AQUA/MODIS/L3M/CHL/2022, Reprocessing.

Nicolaus, M., Katlein, C., Maslanik, J., Hendricks, S., 2012. Changes in Arctic sea ice result in increasing light transmittance and absorption. Geophys. Res. Lett. 39, L24501. http://dx.doi.org/10.1029/2012GL053738.

Onarheim, I.H., Smedsrud, L.H., Ingvaldsen, R.B., Nilsen, F., 2014. Loss of sea ice during winter north of Svalbard. Tellus A 66, 23933. http://dx.doi.org/10.3402/tellusa.v66.23933.

Orkney, A., Sathyendranath, S., Jackson, T., Porter, M., Bouman, H.A., 2022. Atlantic inflow is the primary driver of remotely sensed autumn blooms in the Barents Sea. Mar. Ecol. Prog. Ser. 701, 25–40. http://dx.doi.org/10.3354/meps14201.

Pavlov, V., Pickart, R.S., Sundfjord, A., 2017a. A-TWAIN CTD hydrography September 2012 [Data set]. Norwegian Polar Institute, http://dx.doi.org/10.21334/npolar.2017.5f53146f.

Pavlov, V., Pickart, R.S., Sundfjord, A., 2017b. A-TWAIN CTD hydrography September 2013 [Data set]. Norwegian Polar Institute, http://dx.doi.org/10.21334/npolar.2017.77d58403.

Peralta-Ferriz, C., Woodgate, R.A., 2015. Seasonal and interannual variability of pan-Arctic surface mixed layer properties from 1979 to 2012 from hydrographic data, and the dominance of stratification for multiyear mixed layer depth shoaling. Prog. Oceanogr. 134, 19–53. http://dx.doi.org/10.1016/j.pocean.2014.12.005.

Pérez-Hernández, M.D., Pickart, R.S., Pavlov, V., Våge, K., Ingvaldsen, R., Sundfjord, A., Renner, A.H.H., Torres, D.J., Erofeeva, S.Y., 2017. The Atlantic Water boundary current north of Svalbard in late summer. J. Geophys. Res. 122, 2269–2290. http://dx.doi.org/10.1002/2016JC012486.

Pnyushkov, A.V., Polyakov, I.V., Ivanov, V.V., Aksenov, Y., Coward, A.C., Janout, M., Rabe, B., 2015. Structure and variability of the boundary current in the Eurasian Basin of the Arctic Ocean. Deep Sea Res. I 101, 80–97. http://dx.doi.org/10.1016/j.dsr.2015.03.001.

Polyakov, I.V., Alkire, M.B., Bluhm, B.A., Brown, K.A., Carmack, E.C., Chierici, M., Danielson, S.L., Ellingsen, I., Ershova, E.A., Gårdfeldt, K., Ingvaldsen, R.B., Pnyushkov, A.V., Slagstad, D., Wassmann, P., 2020. Borealization of the Arctic Ocean in response to anomalous advection from sub-Arctic seas. Front. Mar. Sci. 7, http://dx.doi.org/10.3389/fmars.2020.00491.

Polyakov, I.V., Pnyushkov, A.V., Alkire, M.B., Ashik, I.M., Baumann, T.M., Carmack, E.C., Goszczko, I., Guthrie, J., Ivanov, V.V., Kanzow, T., Krishfield, R., Kwok, R., Sundfjord, A., Morison, J., Rember, R., Yulin, A., 2017. Greater role for Atlantic inflows on sea-ice loss in the Eurasian Basin of the Arctic Ocean. Science 356, 285–291. http://dx.doi.org/10.1126/science.aai8204.

Pörtner, H.O., Roberts, D., Masson-Delmotte, V., Zhai, P., Tignor, M., Poloczanska, E., Mintenbeck, K., Alegría, A., Nicolai, M., Okem, A., Petzold, J., Rama, B., Weyer, N. (Eds.), 2019. IPCC Special Report on the Ocean and Cryosphere in a Changing Climate. Cambridge University Press, Cambridge, UK and New York, NY, USA, p. 755. http://dx.doi.org/10.1017/9781009157964.

Previdi, M., Smith, K.L., Polvani, L.M., 2021. Arctic amplification of climate change: A review of underlying mechanisms. Environ. Res. Lett. 16, 093003. http://dx.doi.org/10.1088/1748-9326/ac1c29.

Price, J.F., Welle, R.A., Pinkel, R., 1986. Diurnal cycling: Observations and models of the upper ocean response to diurnal heating, cooling, and wind mixing. J. Geophys. Res. 91, 8411–8427. http://dx.doi.org/10.1029/JC091iC07p08411.

Rainville, L., Lee, C.M., Woodgate, R.A., 2011. Impact of wind-driven mixing in the Arctic Ocean. Oceanography 24 (3), 136–145. http://dx.doi.org/10.5670/oceanog.2011.65.

Rainville, L., Woodgate, R.A., 2009. Observations of internal wave generation in the seasonally ice-free Arctic. Geophys. Res. Lett. 36, L23604. http://dx.doi.org/10.1029/2009GL041291.

Randelhoff, A., Holding, J., Janout, M., Sejr, M.K., Babin, M., Tremblay, J.E., Alkire, M.B., 2020. Pan-Arctic Ocean primary production constrained by turbulent nitrate fluxes. Front. Mar. Sci. 7, 150. http://dx.doi.org/10.3389/fmars.2020.00150.

Randelhoff, A., Reigstad, M., Chierici, M., Sundfjord, A., Ovanov, V., Cape, M., Vernet, M., Tremblay, J.E., Bratbak, G., Kristiansen, S., 2018. Seasonality of the physical and biogeochemical hydrography in the inflow to the Arctic Ocean through Fram Strait. Front. Mar. Sci. 5, 224. http://dx.doi.org/10.3389/fmars.2018.00224.

Randelhoff, A., Sundfjord, A., 2018. Short commentary on marine productivity at Arctic shelf breaks: upwelling, advection and vertical mixing. Ocean Sci. 14, 293–300. http://dx.doi.org/10.5194/os-14-293-2018.

Rantanen, M., Karpechko, A.Y., Lipponen, A., Nordling, K., Hyvärinen, O., Ruosteenoja, K., Vihma, T., Laaksonen, A., 2022. The Arctic has warmed nearly four times faster than the globe since 1979. Commun. Earth Environ. 3, 168. http://dx.doi.org/10.1038/s43247-022-00498-3.

Redfield, A.C., Ketchum, B.H., Richards, F.A., 1963. The influence of organisms on the composition of seawater. In: Hill, M.N. (Ed.), The Sea. John Wiley, New York, pp. 26–77.

Reigstad, M., Cerbule, K., Dubourg, P., Marquardt, M., 2023c. Dissolved inorganic nutrients (nitrate, phosphate and silicic acid) and chlorophyll *a* from the combined Nansen Legacy and A-TWAIN Mooring service cruise November 2019 [data set]. Norwegian Polar Institute, http://dx.doi.org/10.21334/npolar.2023.ca2fa5c5.

Reigstad, M., Øygarden, S., Kristiansen, S., 2023a. Dissolved inorganic nutrients (nitrate, phosphate and silicic acid) and chlorophyll *a* from the A-TWAIN cruise September 2012 [data set]. Norwegian Polar Institute, http://dx.doi.org/10.21334/npolar.2023.18b03a9e.

Reigstad, M., Øygarden, S., Kristiansen, S., 2023b. Dissolved inorganic nutrients (nitrate, phosphate and silicic acid) and chlorophyll *a* from the A-TWAIN cruise September 2013 [data set]. Norwegian Polar Institute, http://dx.doi.org/10.21334/npolar.2023.ad022d35.

Reigstad, M., Wassmann, P., Riser, C.W., Øygarden, S., Rey, F., 2002. Variations in hydrography, nutrients and chlorophyll *a* in the marginal ice-zone and the central Barents Sea. J. Mar. Syst. 38, 9–29.

Renner, A.H.H., Pavlov, V., 2023a. A-TWAIN CTD fluorescence September 2012 [data set]. Norwegian Polar Institute, http://dx.doi.org/10.21334/npolar.2023.2c9e4815.

Renner, A.H.H., Pavlov, V., 2023b. A-TWAIN CTD fluorescence September 2013 [data set]. Norwegian Polar Institute, http://dx.doi.org/10.21334/npolar.2023.5d81157c.

Renner, A.H.H., Sundfjord, A., Janout, M.A., Ingvaldsen, R., Beszczynska-Möller, A., Pickart, R., Pérez-Hernández, M.D., 2018. Variability and redistribution of heat in the Atlantic Water boundary current north of Svalbard. J. Geophys. Res. 123 (9), 6373–6391. http://dx.doi.org/10.1029/2018JC013814.

Rey, F., 2012. Declining silicate concentrations in the Norwegian and Barents Sea. ICES J. Mar. Sci. 69 (2), 208–212. http://dx.doi.org/10.1093/icesjms/fss007.

Rudels, B., Korhonen, M., Schauer, U., Pisarev, S., Rabe, B., Wisotzki, A., 2015. Circulation and transformation of Atlantic water in the Eurasian Basin and the contribution of the Fram Strait inflow branch to the Arctic Ocean heat budget. Prog. Oceanogr. 132, 128–152. http://dx.doi.org/10.1016/j.pocean.2014.04.003.

Rudels, B., Meyer, R., Fahrbach, E., Ivanov, V.V., Østerhus, S., Quadfasel, D., Schauer, U., Tverberg, V., Woodgate, R.A., 2000. Water mass distribution in Fram Strait and over the Yermak Plateau in summer 1997. Ann. Geophys. 18, 687–705.

Sandø, A.B., Mousing, E.A., Budgell, W.P., Hjøllo, S.S., Skogen, M.D., Ådlandsvik, B., 2021. Barents Sea plankton production and controlling factors in a fluctuating climate. ICES J. Mar. Sci. 78 (6), 1999–2016. http://dx.doi.org/10.1093/icesjms/fsab067.

Slagstad, D., Wassmann, P.F.J., Ellingsen, I., 2015. Physical constrains and productivity in the future Arctic Ocean. Front. Mar. Sci. 2, 85. http://dx.doi.org/10.3389/fmars.2015.00085.

Smedsrud, L.H., Muilwijk, M., Brakstad, A., Madonna, E., Lauvset, S.K., Spensberger, C., Born, A., Eldevik, T., Drange, H., Jeansson, E., Li, C., Olsen, A., Skagseth, Ø., Slater, D.A., Straneao, F., Våge, K., Årthun, M., 2022. Nordic Seas heat loss, Atlantic inflow, and Arctic sea ice cover over the last century. Rev. Geophys. 60, http://dx.doi.org/10.1029/2020RG000725, e2020RG000725.

Solomon, A., Heuzé, C., Rabe, B., Bacon, S., Bertino, L., Heimbach, P., Inoue, J., Iovino, D., Mottram, R., Zhang, X., Aksenov, Y., McAdam, R., Nguyen, A., Raj, R.P., Tang, H., 2021. Freshwater in the Arctic Ocean 2010–2019. Ocean Sci. 17 (4), 1081–1102. http://dx.doi.org/10.5194/os-17-1081-2021.

Spreen, G., Kaleschke, L., Heygster, G., 2008. Sea ice remote sensing using AMSR-E 89 GHz channels. J. Geophys. Res. 113, C02S03, http://dx.doi.org/10.1029/2005JC003384.

Stroeve, J., Notz, D., 2018. Changing state of Arctic sea ice across all seasons. Environ. Res. Lett. 13 (10), 103001. http://dx.doi.org/10.1088/1748-9326/aade56.

Sundfjord, A., 2022. CTD data from Nansen Legacy Cruise - Mooring service cruise 2019 [data set]. Norwegian Marine Data Centre, http://dx.doi.org/10.21335/NMDC-2135074338.

Sundfjord, A., 2023c. Nansen Legacy Cruises - Mooring Cruise 2021 [data set]. Norwegian Marine Data Centre, http://dx.doi.org/10.21335/NMDC-499497542.

Sundfjord, A., Reigstad, M., Pavlova, O., Øygarden, S., Beszczynska-Möller, A., Kristiansen, S., 2023a. CTD data and dissolved inorganic nutrients (nitrate, phosphate and silicic acid) and chlorophyll *a* from water samples from the A-TWAIN cruise September 2015 [data set]. Norwegian Polar Institute, http://dx.doi.org/10.21334/npolar.2023.56c1ab00.

Sundfjord, A., Reigstad, M., Pavlova, O., Øygarden, S., Beszczynska-Möller, A., Kristiansen, S., Meyer, A., Muilwijk, M., Renner, A.H.H., 2023b. CTD data and dissolved inorganic nutrients (nitrate, phosphate and silicic acid) and chlorophyll *a* from water samples from the A-TWAIN cruise September 2017 [data set]. Norwegian Polar Institute, http://dx.doi.org/10.21334/npolar.2023.a6b1bc62.

Timmermans, M.L., Marshall, J., 2020. Understanding Arctic Ocean circulation: A review of ocean dynamics in a changing climate. J. Geophys. Res.: Oceans 125, e2018JC014378. http://dx.doi.org/10.1029/2018JC014378.

Tremblay, J.É., Anderson, L.G., Matrai, P., Coupel, P., Bélanger, S., Michel, C., Reigstad, M., 2015. Global and regional drivers of nutrient supply, primary production and CO_2 drawdown in the changing Arctic Ocean. Prog. Oceanogr. 139, 171–196. http://dx.doi.org/10.1016/j.pocean.2015.08.009.

Tuerena, R.E., Mahaffey, C., Henley, S.F., de la Vega, C., Norman, L., Brand, T., Sanders, T., Debyser, M., Dähnke, K., Braun, J., März, C., 2022. Nutrient pathways and their susceptibility to past and future change in the Eurasian Arctic Ocean. Ambio 51, 355–369. http://dx.doi.org/10.1007/s13280-021-01673-0.

Våge, K., Pickart, R.S., Pavlov, V., Lin, P., Torres, D.J., Ingvaldsen, R., Sundfjord, A., Proshutinsky, A., 2016. The Atlantic Water boundary current in the Nansen Basin: Transport and mechanisms of lateral exchange. J. Geophys. Res. 121, 6946–6960. http://dx.doi.org/10.1002/2016JC011715.

Vernet, M., Ellingsen, I.H., Seuthe, L., Slagstad, D., Cape, M.R., Matrai, P.A., 2019. Influence of phytoplankton advection on the productivity along the Atlantic Water inflow to the Arctic Ocean. Front. Mar. Sci. 6:583, http://dx.doi.org/10.3389/fmars.2019.00583.

Waga, H., Hirawake, T., 2020. Changing occurrence of fall blooms associated with variations in phytoplankton size structure in the Pacific Arctic. Front. Mar. Sci. 7, 209. http://dx.doi.org/10.3389/fmars.2020.00209.

Wang, Q., Danilov, S., 2022. A synthesis of the upper Arctic Ocean circulation during 2000–2019: Understanding the roles of wind forcing and sea ice decline. Front. Mar. Sci. 9, 863204. http://dx.doi.org/10.3389/fmars.2022.863204.

Wassmann, P., Kosobokova, K.N., Slagstad, D., Drinkwater, K., Hopcroft, R.R., Moore, S.E., Ellingsen, I., Helson, R.J., Carmack, E., Popova, E., Berge, J., 2015. The contiguous domains of Arctic Ocean advection: Trails of life and death. Prog. Oceanogr. 139, 42–65. http://dx.doi.org/10.1016/j.pocean.2015.06.011.

Wassmann, P., Reigstad, M., 2011. Future Arctic Ocean seasonal ice zones and implications for pelagic-benthic coupling. Oceanography 24 (3), 220–231. http://dx.doi.org/10.5670/oceanog.2011.74.

Wilson, C., Aksenov, Y., Rynders, S., Kelly, S.J., Krumpen, T., Coward, A.C., 2021. Significant variability of structure and predictability of Arctic Ocean surface pathways affects basin-wide connectivity. Commun. Earth Environ. 2, 164. http://dx.doi.org/10.1038/s43247-021-00237-0.

Yentsch, C.S., 1965. Distribution of chlorophyll and phaeophytin in the open ocean. Deep-Sea Res. 12, 653–666.